

University of Tennessee at Chattanooga

UTC Scholar

Honors Theses

Student Research, Creative Works, and
Publications

8-2019

Synthesizing multifunctional iron oxide nanodrugs and developing a model for their size analysis using dynamic light scattering

Olivia George

University of Tennessee at Chattanooga, vtc621@mocs.utc.edu

Follow this and additional works at: <https://scholar.utc.edu/honors-theses>

Recommended Citation

George, Olivia, "Synthesizing multifunctional iron oxide nanodrugs and developing a model for their size analysis using dynamic light scattering" (2019). *Honors Theses*.

This Theses is brought to you for free and open access by the Student Research, Creative Works, and Publications at UTC Scholar. It has been accepted for inclusion in Honors Theses by an authorized administrator of UTC Scholar. For more information, please contact scholar@utc.edu.

Synthesizing Multifunctional Iron Oxide Nanodrugs and Developing a Model for their Size Analysis using Dynamic Light Scattering

Olivia George

Departmental Honors Thesis
The University of Tennessee at Chattanooga
Civil and Chemical Engineering Department

Examination Date: April 1, 2019

Soubantika Palchoudhury
Assistant Professor of Chemical Engineering
Thesis Director

Eleni Panagiotou
Assistant Professor of Mathematics
Department Examiner

Bradley Harris
Assistant Professor of Chemical Engineering
Department Examiner

Table of Contents

I.	Abstract	3
II.	Introduction.....	3
A.	Background & Motivation	3
B.	DLS Background.....	5
1.	Mechanisms of DLS	6
2.	Applying DLS.....	7
C.	Description of Chosen Nanostructures.....	8
III.	Materials and Methods.....	9
A.	Materials.....	9
B.	Synthesis.....	9
C.	Data Collection.....	10
D.	Data Processing	10
IV.	Results and Discussion	10
V.	Conclusions.....	21
A.	Summary of Trends.....	21
B.	Discussion of Project Greater Impacts	21
C.	Future Works.....	21
VI.	References.....	23
VII.	Acknowledgements.....	26
VIII.	Appendix	26
A.	Safety Measures	26
B.	Project Outcomes	27
C.	Raw Data	28

I. Abstract

The growth of targeted drug delivery methods in modern cancer treatments has been the result of an increase in the quantity of drugs available, which is directly affected by the methods used in drug development. These drugs vary in size, shape, and mechanism of operation, so the characterizing techniques used must be adaptable to a variety of particle types. In this thesis, a variety of complex nanostructures were synthesized and characterized using dynamic light scattering (DLS), which is a rapid, non-destructive, and simply-operated size characterization method that does not introduce artifacts from sample preparation. The DLS data was then analyzed to spot trends among the sample varieties that could potentially be used to characterize particle shapes. A foundation was laid for future works developing a computational model to characterize shape based on DLS size distribution data alone.

II. Introduction

A. Background & Motivation

In the United States, cancer is the second leading cause of death overall, triggering 21.8% of 2016 mortalities across all races, genders, and age groups.¹ Accordingly, the scientific community has been hard at work to synthesize an array of solutions, some of which work alone, but many of which are designed to be collaborative with other drugs and treatment methods.² Thanks to these constant improvements in treatment methods, between 1999 and 2015, cancer rates decreased 1.4% in women and 1.8% in men.³ These methods range from vaccines to adoptive T-cell therapy and can be combined, like with radiation and CTLA-4 to treat melanoma or, as in a study by Pathak, et al., by combining an array of chemotherapeutics with anti-inflammatory agents, and radiation to build its multimodal therapy.^{2,4} In particular, a great deal of research has been done recently to develop methods of targeted drug delivery, a promising treatment method that has the potential to increase the potency of the treatment without increasing the side effects the patient must endure.⁵

In targeted drug delivery, the mechanism of targeting varies from type to type, but the core process is the same: a nanoparticle is synthesized with properties designed to leverage the weaknesses of tumors. These nanoparticles (NPs) can be designed to change shape or size with a change in pH, to increase the quantity of reactive oxygen species within the tumor cells in response to light, or to modify the DNA of the cancer cells, among many other possible

mechanisms.^{2,4-7} A constant across all of these mechanism types is the importance of NP size; in creating NPs for targeted drug delivery purposes, NP size is one of the most important factors to consider, as it directly impacts the success of the treatment.⁸⁻¹¹ If the NP is smaller than 20nm in diameter, the immune system can easily dispose of the particle; if the NP is larger than 200nm in diameter, it is too large to enter tumor vasculature, disrupting the mechanism of most targeted drug delivery treatments.^{11,12} Thus, accurate characterization of NP sizes is a cornerstone for targeted drug delivery treatment development.

Successful characterization of NP size is simple for spherical particles, for which there are a number of characterization options, including various cheap and simple-to-use methods involving light scattering.^{9,13-15} However, there is a growing need for accurate size characterization of non-spherical NPs, as these NPs can be the product of hybrid or multi-component NPs which are tailored to more effectively accomplish a specific purpose.^{5,16-21} There are several advantages to choosing non-spherical NP shapes, not least of which being their customizable nature.^{5,7,12,22-24} Multiple sub-particles can be combined to make the treatment NPs, resulting in structures like those shown below in Figure 1.

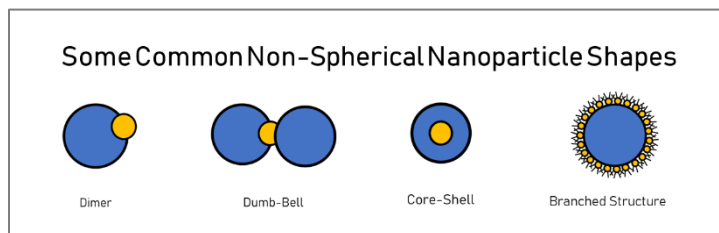


Figure 1 – Some of the most common and useful non-spherical NP shapes^{19,25-28}

By combining multiple sub-particles, the final NPs can be tailored to have specific desirable traits, such as pH responsiveness, photosensitivity, and high levels of reactivity.^{10,29-32} These traits can work together to effectively eliminate the tumor cells. Without accurate size characterization methods, successfully developing these non-spherical NPs to fall within the specified size range can be difficult if not impossible, since size is one of the most fundamental factors in a NP treatment's success in infiltrating the tumor cells.

In characterizing non-spherical NPs, one of the most effective and popular methods is transmission electron microscopy (TEM).^{28,33,34} Although TEM is a powerful tool for conclusively determining the shapes of NPs, the instruments can cost over \$100,000, they are

time consuming to use (which limits the quantity of data that may be processed for a given sample), they are destructive to the sample, and they only provide 2-dimensional analysis of the particle shapes.³³ Although such equipment has proven indispensable in the high-level research involved in finalizing a cancer drug, more preliminary research does not require such precision. In fact, since many research groups do not have access to the state-of-the-art equipment afforded to large Research I universities and national labs, these groups are limited to performing preliminary research with simple equipment setups. In these research settings, even though there is not access to such equipment as the above, the research performed is still held to the same standards for validity, putting smaller research groups at a stark disadvantage. However, it is possible that with the right tools, these groups could still produce meaningful research without requiring prohibitively expensive equipment. Additionally, DLS is advantageous because exactly the same sample may be measured repeatedly with no sacrifice in sample quality. DLS also does not require any significant sample preparation; TEM however requires that samples be put on a slide, which eliminates the sample for repeated use, and may require the use of cell staining, which introduces an additional variable to the experiment.

For spherical nanoparticles, dynamic light scattering (DLS) is a cheap and reliable method of size characterization that is common, if not fundamental, in most nano-scale characterization labs. If a computational model could be created to work in tandem with DLS size measurements to navigate the complexities of NP shape, such a model would likely be indispensable for many of the mentioned smaller nano-scale characterization labs. The purpose of this thesis is to set the experimental foundation for a larger project which will attempt to establish the suggested model by analyzing the DLS size characterization outputs for a selection of similar but varying non-spherical NPs, detecting any trends apparent from the data, and using the data as a basis for the computational model.

B. DLS Background

Dynamic light scattering (DLS) is the preferred characterization method for this project because it requires minimal sample preparation and does not modify the sample by taking a measurement, unlike other characterization methods which can require time-consuming preparation techniques and may employ destructive mechanisms of characterization.^{9,15,35} Additionally, DLS instruments are generally cheap to operate, requiring only electricity, and are cheaper than some higher end characterization instruments, such as transmission electron

microscopy (TEM) and freeze-fracture electron microscopy.^{15,35} These reasons combine to mean that DLS characterization is one of the most financially and operationally approachable methods for small labs and would thus be best suited to achieve the goal of this project.

1. Mechanisms of DLS

In short, DLS works by shining a laser through a liquidous sample of NPs, recording how the light scatters, and using that information to computationally determine the size (or zeta potential) of the sample. The instrument takes advantage of the random motion inherent to any particle above the temperature absolute zero; this random motion is known as Brownian Motion.^{9,13,14,34} The speed of the Brownian Motion exhibited by a particle is directly related to the particle's size. The smaller the particle, the faster it moves among the particles of the solvent; similarly, the larger the particle, the slower it moves among the solvent particles.^{9,13} This relationship is mathematically defined by the Stoke-Einstein equation, shown below as Equation 1.^{9,13}

$$d_H = \frac{k_B T}{3\pi\eta D} \quad [1]$$

In this equation, k_B is the Boltzmann constant, which equals 1.38064852E-23 J/K, T is the temperature, η is the absolute viscosity, D is the translational diffusion coefficient, and d_H is the hydrodynamic diameter. With T known, the sample's viscosity can be determined, which only leaves the diffusion coefficient to be measured by the DLS instrument. This value is measured using some type of photon counting device, which is often positioned at a 173° angle from the laser entering the sample, the setup required for backscatter detection.¹³ The photon counter is directly connected to a correlator, which converts the raw intensity data of the scattered light into size data using cumulant and distribution analysis. The cumulant analysis obtains overall data such as the mean size (denoted z-average) and sample polydispersity index (PDI); the z-average value calculated by cumulant analysis is less applicable for more disperse samples.^{9,13} Distribution analysis, however, accounts for the whole spread of intensity data across the measured range of particle sizes. The raw data is converted to usable peaks via distribution algorithms; the algorithm used in this project was the general purpose algorithm, which works best for samples of unknown shape and size distributions.¹³ The size distribution data can be converted to three forms: intensity, volume, and number.

The intensity-based size distribution graph can be directly created from the collected light intensity data, which is why many consider it the primary form of DLS size data, with volume and number distributions only used relatively.^{9,13,14} However, since the intensity data is collected by measuring the speed of variation in photon reflection, larger particles that move slower can have a lasting effect on the recorded intensity, causing the intensity distribution to weight heavily towards the larger particles.^{9,13} Thus, there is still value in the volume and number distributions, even though those must be derived from the intensity data using the approximate model established by Mie theory. This model requires knowing (or approximating) the particle absorption and particle refractive index values in order to find the volume and number distributions.^{9,13–15} Once calculated, the volume distribution corresponds to the mass distribution of the NPs across the size range, and the number distribution corresponds to the count of NPs across the size range.¹³

2. Applying DLS

In order to lay a foundation for how DLS could be combined with computational analysis to provide approximate particle shape data, it is necessary to review how light scattering techniques have been used in previous studies to obtain particle shape.

A study by Pencer, et al. used DLS in combination with static light scattering (SLS), which characterizes a sample by measuring the light scattering at a variety of angles, rather than over time, like DLS.^{14,15} This study focused on the shape characterization of pure lipid membranes called vesicles and determined that “a combined analysis of SLS and DLS data provides a unique determination of vesicle shape, size, and size distribution”.¹⁵ Another study by Martchenko, et al., which used magnetic NPs similar to those used in this project, used TEM to determine the particle shape and thus the corresponding hydrodynamic model to apply in order to obtain the translational and rotational diffusion coefficients from the DLS data.²¹ A study by Abdelmohsen, et al. used a combination of multi-angle light scattering (MALS) and quasi-elastic light scattering (QELS) (both of which operate on many of the same principles as DLS) to characterize the shapes of sphere, disc, and rod-shaped NPs; their study also used TEM and cryogenic-TEM to establish the NP shapes to best confirm the results of the light scattering characterizations.³⁶ Additionally, a study by Zheng, et al. examined the reliability of DLS as a characterization technique, establishing that factors such as sample concentration and the incident laser power can significantly alter the intensity and size data collected by the DLS.³⁵

It is important to note that in none of the reviewed applications of DLS in shape characterization was it used alone. In these past studies, DLS has always been paired with other characterization methods to either create or confirm shape data. However, the purpose of this project is to investigate how DLS might be used as a stand-alone characterization, paired only with post-characterization computational analysis of the intensity, number, and volume distribution data as well as the cumulant analysis collected.

It is hypothesized that by studying values such as the polydispersity and the distribution of peaks in the intensity, number, and volume plots, the DLS data could be self-sufficient in providing approximate particle shape data.

C. Description of Chosen Nanostructures

In this study, the NPs analyzed were core-shell hybrid NPs made of an iron oxide (IO) core surrounded by a layer of polyethyleneimine (PEI) to change the IO core from hydrophobic to hydrophilic so it could best bond with the outermost layer of precious metal, either Pt or Au. These NPs were made as representative samples of non-spherical NPs. The core-shell structure lends itself to more spherical NP shapes, so it was expected that these NPs would be better suited to approach the challenges of shape characterization than particles with less regular shapes. Additionally, these NPs are already being tested for a variety of applications, including plant fertilization, catalysis, and targeted drug delivery. In particular, the targeted drug delivery applications for these NPs are of interest because of the critical size constraints that limit the NPs. In brief, if the NPs are smaller than 20nm in diameter, the immune system can easily dispose of them; if the NPs are larger than 200nm in diameter, they are too large to enter tumor vasculature, which prevents them from carrying out the intended therapy.^{11,12}

In addition to the primary purpose of this thesis, which is to lay the foundation for a computational method of shape characterization using DLS data, a secondary goal is to manipulate these hybrid NPs and observe the DLS data for trends. It was suspected that the proportion between the volume of IO and the volume of Pt or Au added to the NP synthesis would impact the final size and/or shape of the NPs. Accordingly, the samples were made with varying IO:Pt/Au proportions. Below, Table 1 details the proportions chosen and the volumetric concentration of Pt or Au in each sample.

Table 1 – The given names and proportion for the samples created for this thesis

Name	IO Stock	1:100	1:50	1:25	1:10	1:5	Reduced
Pt/Au:IO Proportions	0:1	1:100	1:50	1:25	1:10	1:5	1:0
Concentration % of Pt/Au	0%	1%	2%	4%	10%	20%	100%

Table 1 defines the composition for all of the samples that were created for this thesis project; although an attempt was made to ensure the figures are clear about the compositions of the samples to which the data refers, it may still be helpful to reference Table 1 for ultimate clarity.

III. Materials and Methods

A. Materials

The materials used were as follows: iron(III) acetylacetonate ($\text{Fe}(\text{acac})_3$, 99%, Alfa Aesar), hexane (99%, Sigma-Aldrich), polyethyleneimine (PEI, Mw 60 kDa, 50% aq., Alfa Aesar), deionized (DI) water, platinum (Hexachloroplatinic(IV) acid solution about 10%, 3.8% Pt, Sigma-Aldrich, and gold (Gold (III) chloride hydrate, 99.99%, Sigma-Aldrich).

B. Synthesis

The iron oxide (IO) core-shell NPs were built from a phase-changed solution of iron oxide nanospheres. To create that phase-changed solution, first an organic-phase solution was created by mixing 1 part by volume IO NPs (already created using thermal decomposition, as described in published literature) to 25 parts by volume hexane (99%, Sigma-Aldrich), then sonicating the solution for 10 minutes²⁴. To change the phase of the iron oxide nanospheres from hydrophobic to hydrophilic, 1mL of the organic-phase iron oxide nanosphere stock solution plus 0.5g PEI (polyethyleneimine) plus 5mL DI water in a 20mL vial, sonicated for 1 hour. After letting the solution sit for 1 day, the water-soluble solution was retrieved from under the top organic layer.^{23,37–39}

Next, the Pt and Au stock solutions must be made in preparation for the hybrid NP synthesis. For the Pt stock solution, 0.1mL of the H_2PtCl_6 solution, as-is from Sigma-Aldrich, was added to 5mL of DI water, and the solution was mixed under UV light for 30 minutes. For the Au stock solution, 0.005g of $\text{HAuCl}_4 \cdot x\text{H}_2\text{O}$ was added to 5mL of DI water and mixed well.

Once the phase-change solution has been created, the Pt-IO and Au-IO hybrid NPs can be synthesized. To synthesize the hybrid NPs, first the phase-changed IO NP solution was sonicated for 10 minutes, then 0.5mL of it was combined with 0.1mL of the stock solution of either Pt or Au, depending on which hybrid NPs were being made. The vial was put onto a rotator and rotated under UV light for 30 minutes.^{17,24}

In making the hybrid NPs, the ratio of the volume of Pt/Au used to the volume of the phase-changed IO solution used was varied according to Table 1, above.

C. Data Collection

Once the samples were synthesized, the size data of each sample was collected using the Litesizer 500 particle analyzer (Anton Paar) at room temperature. The Litesizer operates using dynamic light scattering (DLS), as described in the introduction above. For each sample, the size data was collected at least three times, with additional measurements taken as necessary to account for potentially erroneous data.

To test for sample stability over time, some samples were re-measured 1.5 months after their synthesis and initial measurement. In these instances, the samples were sonicated for 10 minutes each prior to the measurement of the sample; all samples were measured in triplicate.

D. Data Processing

The data was processed using Microsoft Excel, making particular use of the Query, Pivot Table, and Pivot Chart functionalities of the program to consolidate the individual spreadsheets made with each new DLS measurement. Sets of data for the same sample taken on the same day were averaged together, and the data were analyzed for trends using the intensity, volume, and number types of DLS size analysis.

IV. Results and Discussion

The DLS measurements of the samples specified in Table 1 were taken in a random order and in triplicate. Additionally, some of the measurements were taken on two separate days, months apart, to analyze how the NP sizes are impacted over time. In Table 2 below, the overall average hydrodynamic diameters and polydispersity indices (PDI) are recorded, created by averaging all the measurements taken for each sample, across dates (averaging fresh and aged sample data together).

Table 2 – A summary of the hydrodynamic diameters and polydispersity indices found for each sample.

	Au		Pt		Iron Oxide Stock	
Pt/Au Concentration	Hydrodynamic diameter (nm)	PDI (%)	Hydrodynamic diameter (nm)	PDI (%)	Hydrodynamic diameter (nm)	PDI (%)
0%					327.22	21.15
1%	212.50	25.63	357.05	24.30		
2%	209.04	26.08	195.00	25.71		
4%	192.63	25.59	203.77	26.96		
10%	154.93	25.04	241.92	27.44		
20%	157.02	24.84	189.41	24.67		
100%	23354.50	38.57	32485.24	40.18		

In Table 2, it is important to note that with the exception of the 100% Au and 100% Pt samples, the PDI is below 30%, meaning that the overall variation in the sizes of the NPs per sample was never more than the maximum variation acceptable for the application.

The 0% Pt/Au concentration data was collected by conducting the same synthesis process as used to create the Pt-IO and Au-IO hybrid NPs but without adding Pt or Au, creating the core IO NPs alone. These NPs were characterized using the DLS. Figure 2, right, presents the intensity, volume, and number-based charts depicting the distribution of the particles along the various hydrodynamic diameters. Notice that the sizes detected are mostly uniform, ranging from approximately 130nm to 690nm for all three distributions. This uniformity of peaks is valuable in characterizing the Pt/Au hybrid NPs because it indicates that the IO NPs alone will not aggregate beyond the shown size range. Additionally, these sizes are larger than the sizes shown below in the hybrid NPs, suggesting that the interactions between IO and Pt/Au limit the aggregation of the hybrid NPs, tailoring the size to be smaller.

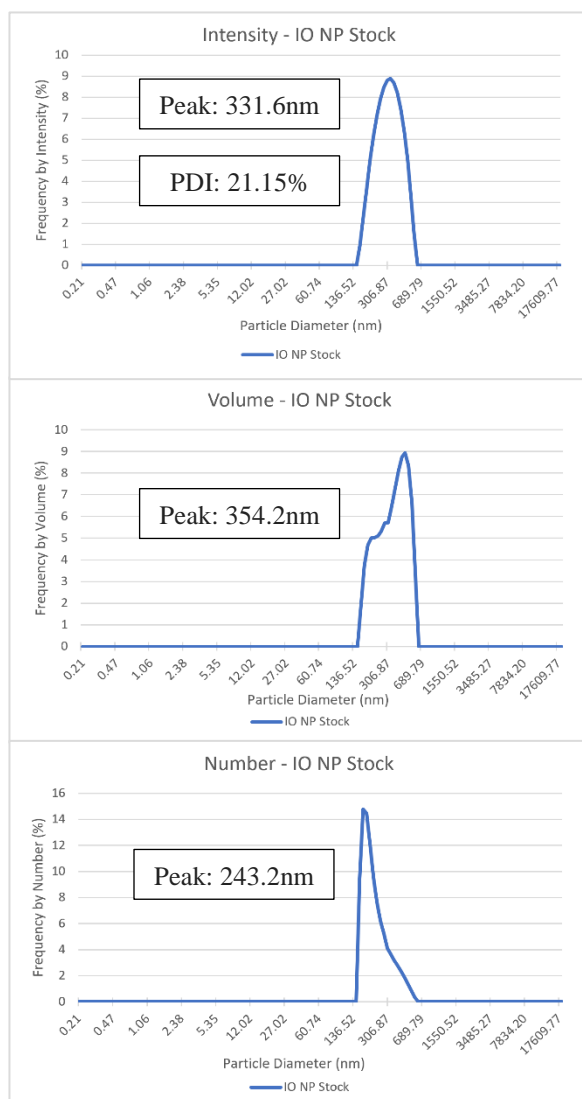


Figure 2 – Hydrodynamic diameter distributions of seed iron oxide NPs

It was also valuable to analyze the trends in the peak and average sizes for each sample with regards to intensity, volume, and number measurements. The peak measurements were determined as the NP size with the highest associated intensity, volume, or number, respectively. The average sizes for each sample were determined using the cumulative data for each sample, which listed the D10, D50, and D90 sizes, correlating to the 10%, 50%, and 90% points along a standard distribution curve of the diameters measured. Thus, the D50 values represent the average hydrodynamic diameter values determined by the root intensity data. To most clearly represent the differences between the peak hydrodynamic diameter values and the D50/average values, this data was graphed for the intensity, volume, and number values as a trend against the changing concentration of either Pt or Au right in Figure 3.

In Figure 3, it is clear to see that although the specific values found for each individual concentration varied a bit between the D50 and the peak sizes, the trends across all of the samples were very similar for the D50 and peak size data. That similarity indicates that the average sizes of the range of particle sizes is close to the particle sizes with the highest intensity of laser scattering, which suggests that the particle sizes are fairly

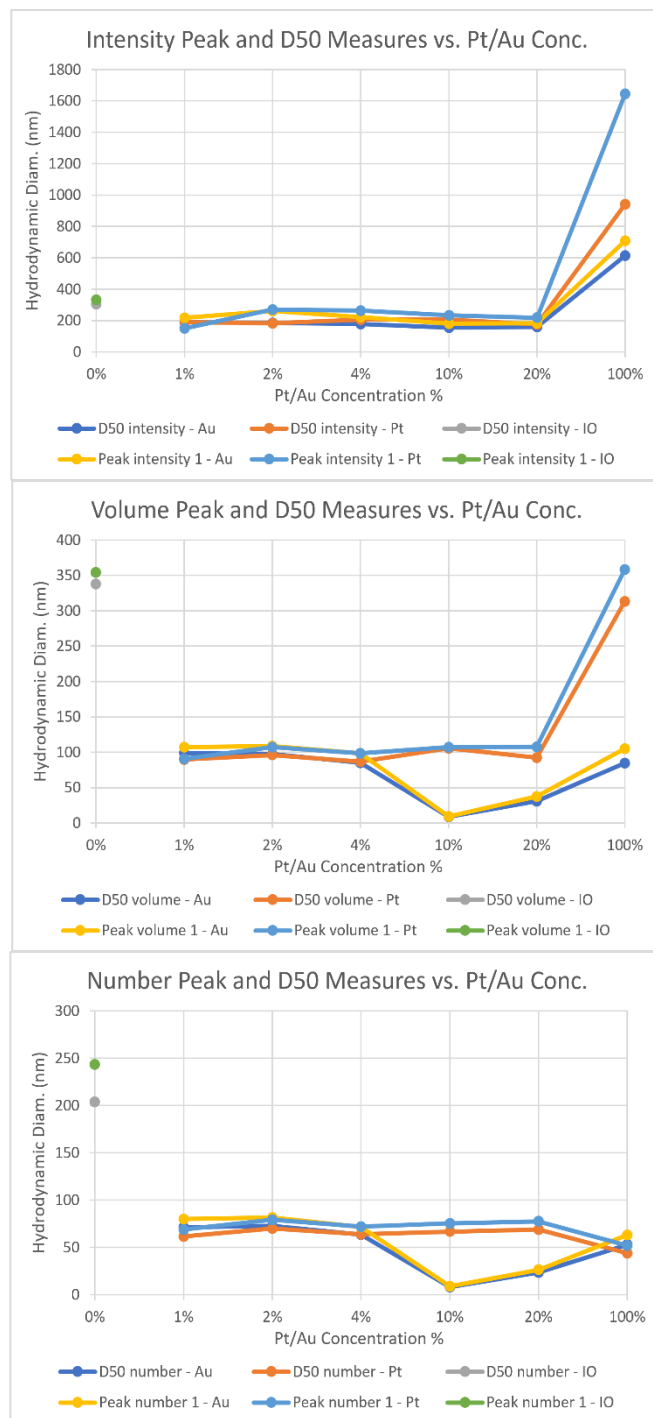


Figure 3 – Trends in the intensity, volume, and number-based peak and average particle measures, correlating to the concentration of Pt or Au in each NP sample

normal in their distributions. Statistically normal distributions of hydrodynamic diameters suggest that the sizes measured are likely uniform overall and may be close to spherical. It may be speculated that non-spherical particles would result in a multi-peak size distribution, with one peak representing the hydrodynamic diameter associated with one major dimension, and the other peak(s) associated with the other dimension(s).

The data shown in Table 2 and Figure 3 is important for describing overall trends in the sample set. However, it is also important to become more familiar with trends in the individual samples, since these individual sample trends are what will eventually be used to determine the shape of the NPs through computational means. In particular, the standard deviation of the size distribution data is an indicator of the consistency of the size peak data.

Below, Figure 4 shows how standard deviation changes over the range of particle sizes determined by intensity, volume, and number data. The error bars represent the standard deviation, calculated by comparing the value for each point across the three trials for the Au reduced NPs.

By looking at the charts in Figure 4, a clear correlation can be drawn between the intensity, volume, and number distributions, especially regarding the peaks at approximately 1nm, the “small” peak, and the peaks ranging from approximately 300-3000nm, the “large” peak. Notice that the relative frequency % for the “small” peak increases going from intensity to number, while the frequency % for the “large” peak decreases. This change supports the hypothesis that the intensity chart would most emphasize the large particles while the number chart would most emphasize the small particles.

When considering how to characterize the shapes of the NPs described by Figure 4, all three distributions must be considered collectively. For instance, on the number distribution, look at the peaks at approximately 140nm and 650nm. These peaks indicate that these sizes had relatively high counts compared with neighboring sizes. In the volume distribution, these same sizes show up only as subtle peaks, indicating that although there may have been a relatively large number of particles with these hydrodynamic diameters, these particles did not substantiate more of the volume of the sample than did other sized particles. Moving to the intensity distribution, it appears that particles with hydrodynamic diameters around 140nm and 650nm are merely part of a larger trend, indicating that the collective population of large particles created

the wide peak, irrespective of the volumetric quantities or counts of the constituent particle sizes. The high standard deviations seen in the intensity distribution are likely a reflection of the inconsistent photon reflections that created the intensity curve shown. In fact, the standard deviations above particles with hydrodynamic diameters of approximately 200nm and higher are generally larger standard deviations than most other standard deviations shown (the exception being in the volume distribution, where the measured frequency % of volume associated with the small NPs varies significantly more than that associated with the large NPs). This increase in standard deviation suggests that particles above 200nm in hydrodynamic diameter may be exhibiting aggregation.

It is worth remembering that the sample analyzed in Figure 4 is one of the two 100% concentration samples; these samples have the highest variability in sizes and may be concluded to have the highest particle aggregation. Thus, although the Au Reduced NPs sample shown in Figure 4 is a good

example of how standard deviation can impact the conclusions made about a size distribution, that sample is not representative of the types of trends evident in other samples. For an example that is more characteristic of the peaks and standard deviations found with a typical sample, Figure 5 below shows how the 1:5 Au:IO sample compared over the span of approximately 1 month of aging. Shortly before collecting the data, the sample was sonicated for 10 minutes to

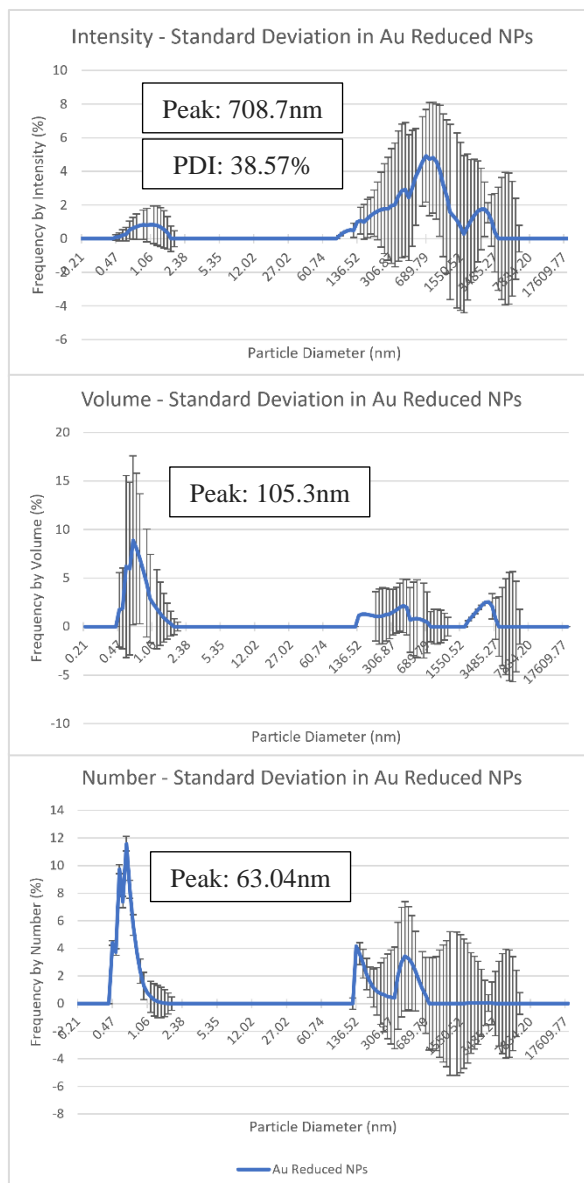


Figure 4 – visualization of the standard deviation trends across the range of particle sizes using intensity, volume, and number data for the Au reduced NPs

reintegrate any particles that may have fallen out of solution or settled to the bottom of the sample; sonication was standard practice for characterizing samples over 1 week old.

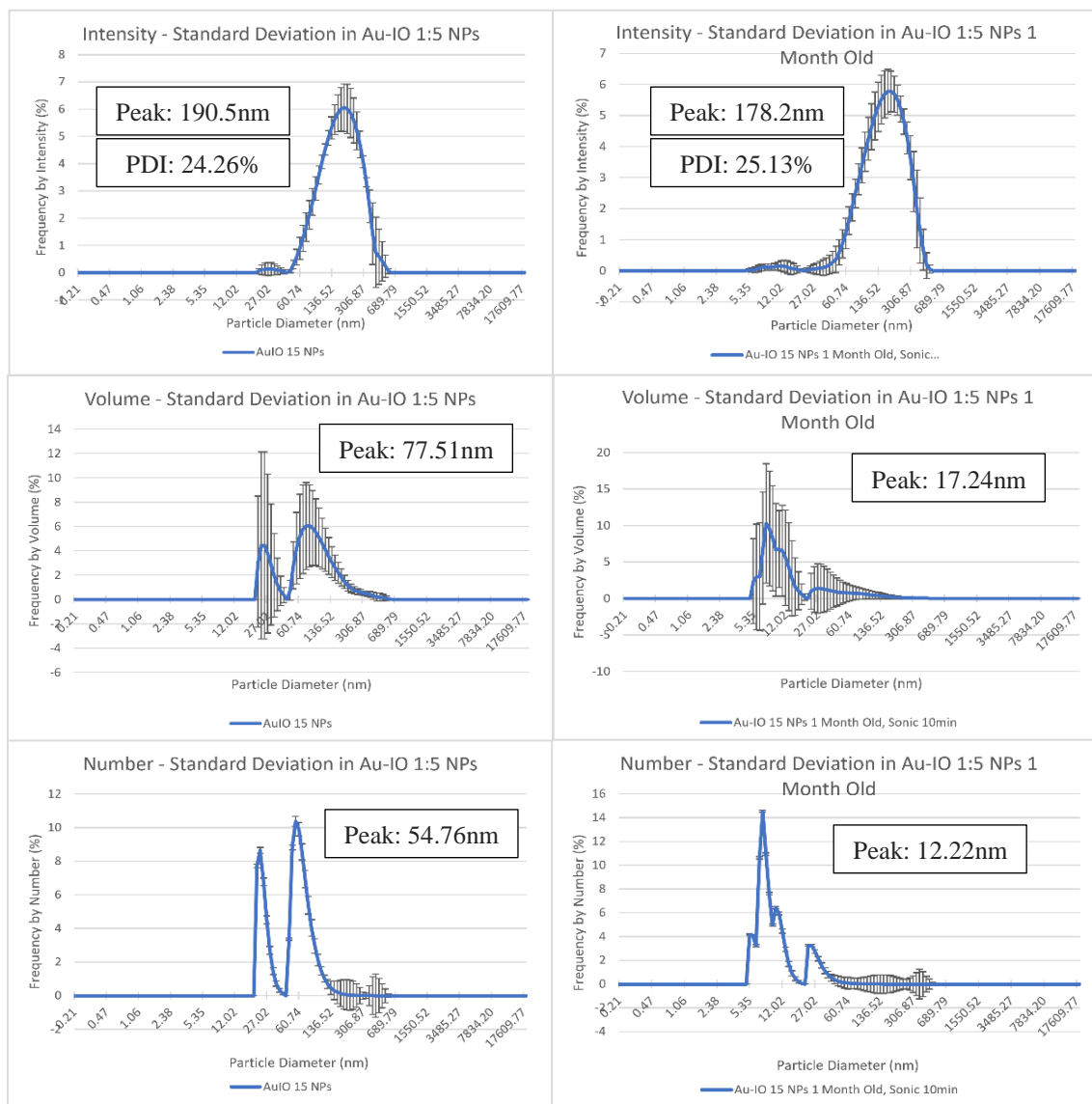


Figure 5 – The impacts of time on the size distribution and standard deviations for the 1:5 Au-IO sample

Above in Figure 5, the overall intensity distribution curve did not change shape or shift after the time delay, indicating that the samples likely maintained their sizes over the month. The volume curves show that after the month of aging, the mass fraction of NPs attributed to the larger original peak decreases to almost nothing. Similarly, the number count of particles in the larger size peak goes down significantly, causing the peak associated with the smaller NPs to have a higher percent frequency. These decreases in larger sizes could be an indication of the

aging process of the samples but could also be related to something about the method of characterizing the samples. Sonication in particular may be the step that decreases the size of larger particles. Through agitating the sample using sound waves, sonication increases the number of particle-particle interactions, which can break down larger particles or cause aggregation, depending on the particles in question.¹³ The trends in Figure 5 suggests that for these NPs, sonication breaks down the larger particles. Focusing on the DLS data from the day the sample was new (left), again it is clear that the intensity distribution weights the largest particles the most while the number distribution weights the smallest particles the most. All three distributions have a peak around the 136nm tick mark, but going from intensity to volume to number, the value for the peak hydrodynamic diameter decreases with each distribution. The clear bimodal distribution seen in the volume and number graphs suggest that these may be either two distinct particle sizes or two dimensions of a single type of non-spherical particle. It was hypothesized that the curve observed for the different dimensions of a non-spherical particle would have a higher minimum frequency in between the two peaks, since the light scattering occurring when the particle is at an unusual angle relative to the laser would likely determine a hydrodynamic diameter between the sizes of the primary dimensions. Thus, it may be supposed that the bimodal distribution in Figure 5 corresponds with two distinct NP sizes in the sample, prompting questions about how and why such a distribution occurs.

To better tell whether the observed trends in Figure 5 are specific to the Au IO NPs or are also part of the Pt IO NPs distributions, look to Figure 6, below, which compares the 1:5 Pt IO sample data when the sample was fresh and when the sample was over 1 month old.

Similar to the data shown in Figure 5, in Figure 6 it is observed that the aged 1:5 Pt IO sample produced almost the same size distributions as the original. In total, the main differences from month to month was the growth of the peak at approximately 2000nm, which differs from the 1:5 Au IO sample, which decreased in large particle peak frequencies. The peak at approximately 2000nm is evident most in the intensity and volume distributions but is also visible to a lesser extent in the number distribution. This increase in larger particles means the NPs are aggregating over time, though not significantly. Though, as with the Au IO NPs, it may be speculated that the sonication step prior to characterizing old NPs may be causing changes to

the samples, specifically aggregation in this case. If further aggregation is observed, it may be worthwhile to try filtering the samples to remove aggregates prior to measurement or use.

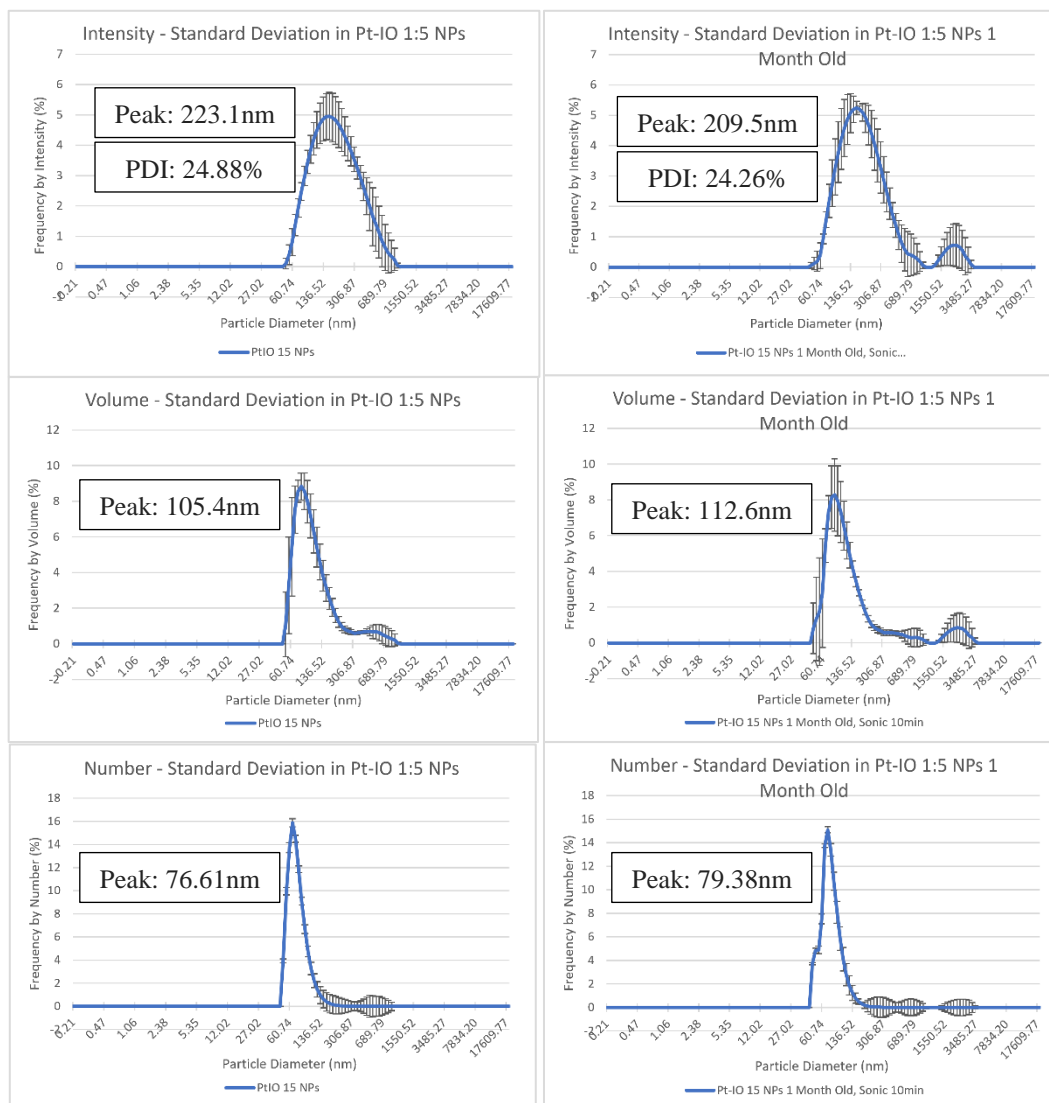


Figure 6 - The impacts of time on the size distribution and standard deviations for the 1:5 Pt-IO sample

In an effort to investigate the impact of sonication on the characterization of the Au-IO and Pt-IO 1:5 samples, these samples were characterized approximately 4 months after their synthesis, first without sonication, then again after 10 minutes of sonication. Below, Figure 7 depicts the Au-IO 1:5 sample data at 4 months old, both with and without sonication.

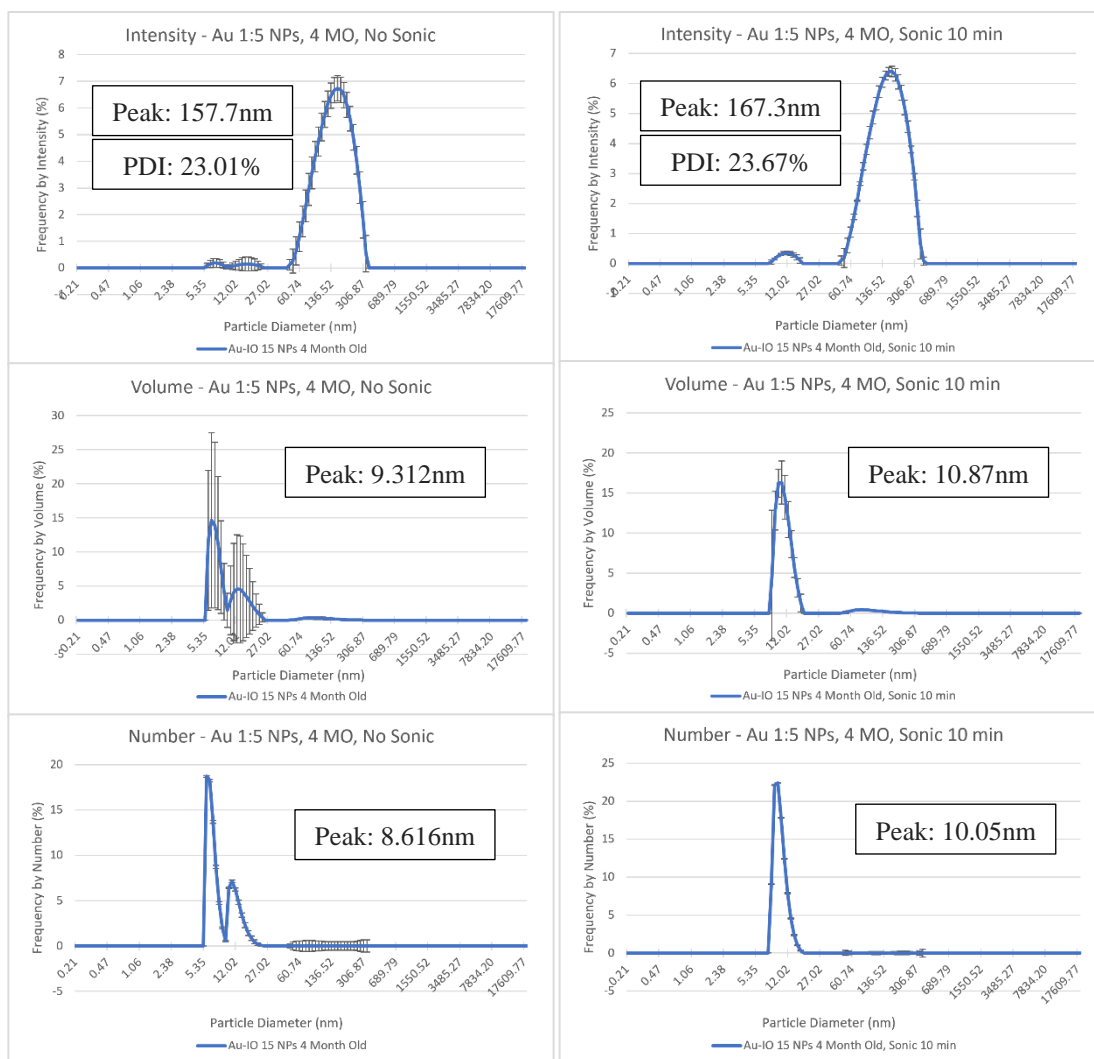


Figure 7 – The impact of sonication on a 4 month old sample of the 1:5 ratio Au-IO NPs

Upon observing the distributions in Figure 7, it appears that sonication helps the Au-IO NPs go from generally bimodal distribution to almost single peaks. This is particularly evident in the volume and number distributions, both of which exhibited clear bimodal distributions in the no sonication graphs but also showed up as a single peak after sonication. It is worth noting that the variation, as depicted by the standard deviation error bars, decreases for all three distributions. This overall decrease in sample variation was unexpected; it appears that the process of sonication leads to more consistent NP sizes and/or shapes. Currently, there is not enough data to suggest a reason why the sonication functioned in this way, so further exploration will have to be pursued with future samples.

When comparing Figure 7 with Figure 5, which depicts the fresh and 1 month old characterization data of the same sample, it seems clear that the NPs are decreasing in size over time. For example, the size with the highest intensity frequency % in the fresh NPs was 190.5nm in hydrodynamic diameter, 178.2nm at 1 month old, and 157.7nm at 4 months old. Similarly, the size with the highest volume frequency % goes from 77.51nm in the fresh NPs to 17.24nm after 1 month and 9.312nm after 4 months, decreasing in size by 88% over the course of those four months. Similar trends are observed in the number-based distributions. These trends indicate that the aging of the NPs almost certainly results in the shrinkage of the NPs. Since the sonicated vs. not-sonicated distributions showed peaks with ranges more similar than those of the fresh NPs, it may be believed that the Au-NP shrinkage occurs due to aging rather than because of sonication. However, given the change from bimodal to single-peak distribution, it is clear that sonication does alter the sample in some way that is yet to be fully understood.

To determine if sonication is the causal factor in the size increases in the Pt-IO 1:5 sample, additional characterization was also conducted on the sample, also at approximately 4 months after the original sample synthesis. This data is shown below in Figure 8. Overall, these distributions are almost identical. The primary differences are the higher frequency %'s at sizes around 690nm in the sonicated samples that were not there in the non-sonicated samples. It may then be speculated that the sonication step caused low levels of aggregation in the sample, but an observation from the laboratory suggests otherwise. It was visually observed that not all of the 1:5 Pt-IO sample was retrieved from the plastic vial (visible in Figure 9 in the Appendix) due to the limitations of the disposable pipet used. The last drop remaining in the vial had floating particles large enough to be seen by the unassisted human eye; these particles were not observed to be present in the tested portion of the sample. After the non-sonicated data was collected, the sample was returned to the vial and sonicated for 10 minutes. When the sample was removed from the vial again, the final drop of sample appeared uniform with the tested portion of the sample. Because of these observations, it appears that the increase in larger particle prevalence with the addition of the sonication step had more to do with including existing large particles than it had to do with causing aggregation. It would be beneficial to repeat this test with an additional filtering step before the measurements occur to eliminate existing large particles. Alternatively, returning the sample to its original vial could be avoided, ensuring that the original tested sample is exactly the same sample as the sample tested after sonication.

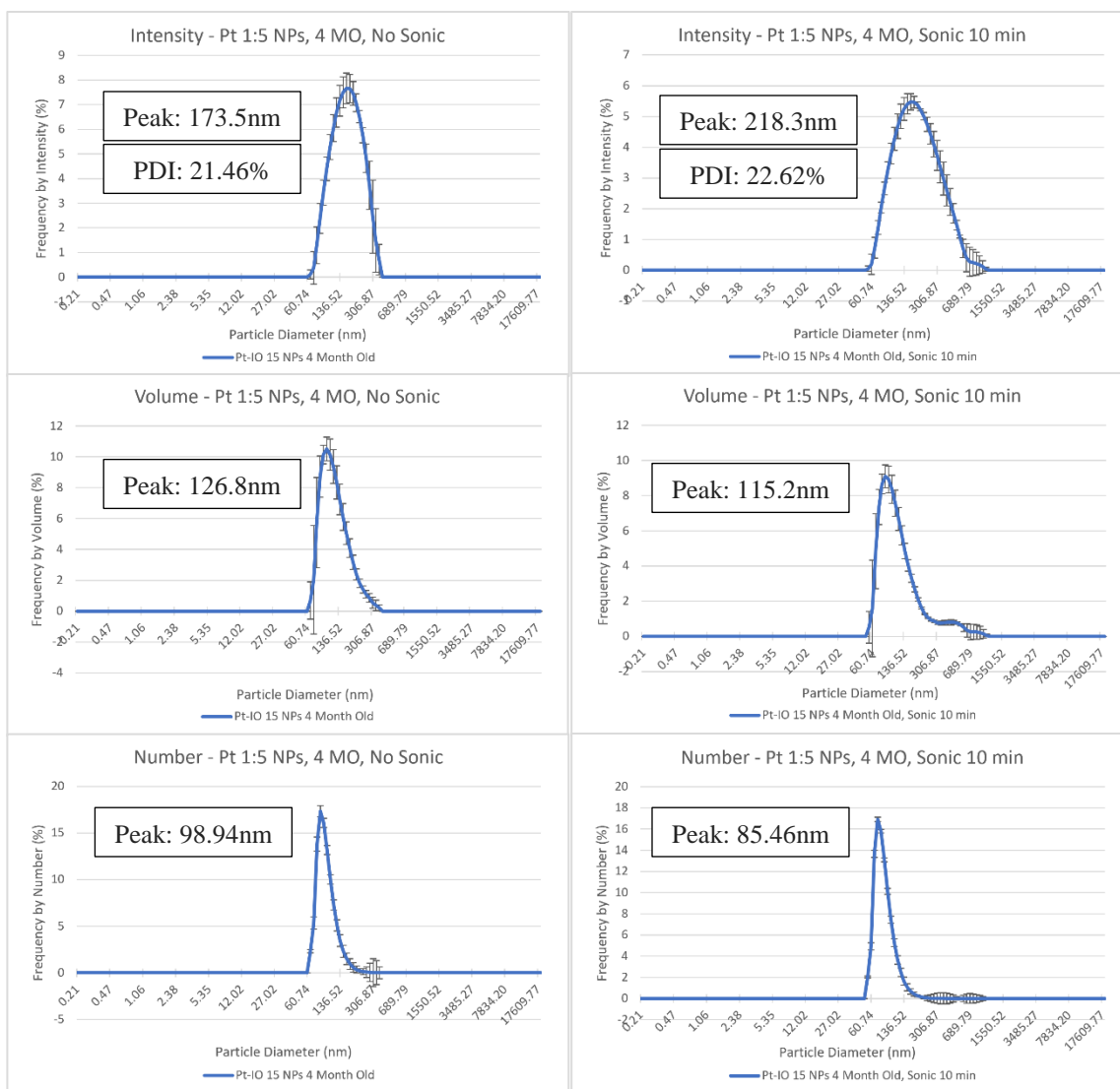


Figure 8 - The impact of sonication on a 4 month old sample of the 1:5 ratio Pt-IO NPs

In comparing Figure 8 to Figure 6, it appears that the 1:5 Pt-IO NPs did not change much over time. The distributions are very similar from the first test to the last, although there does seem to be a shift to the larger sizes by about 20nm. Additionally, the overall standard deviation appears to decrease in the sample. These changes suggest that the process of aging causes the 1:5 Pt-IO NPs to slowly aggregate, potentially unifying the size and shape of the particles in the sample, with the exception of the aggregated NPs. Further research will be required before conclusions may be made regarding this data and the impact of aging or sonication on the NPs.

Beyond the three samples depicted in Figures 4-8, an overall analysis could be made by computational means to help create a full, statistically-sound analysis of the data. However, due

to time limitations, this analysis will be delayed until the computational side of this project is completed. This analysis may benefit from comparing the standard deviation at sample peaks with the sizes associated with those peaks. Peaks with small error bars indicate a consistent size of NP included in the sample, while peaks with large error bars may be evidence of aggregation or non-spherical NPs. Furthermore, if the sample is assumed to have mostly uniform particles, it may be assumed that different peaks represent the hydrodynamic diameters of the different dimensions of the NPs, which will be a helpful principle in determining NP shape through computational methods in future work.

Additional figures with standard deviation distributions, overall intensity, volume, and number size distribution curves, and concentration-related trends in overall or average data values can be found in the Appendix.

v. Conclusions

A. Summary of Trends

In total, the data collected shows that the sizes of the NPs are generally consistent over time, and the intensity, volume, and number distributions show few peaks overall, indicating that the sample NP hydrodynamic diameters do not vary significantly. This speculation based on the number of peaks is supported by the PDI's found, which are all relatively low except for the pure Pt/Au samples, which exhibited higher dispersity likely due to aggregation. Because of the way the intensity, volume, and number distributions work, the intensity size distribution curves are most effective at identifying large particles, and the number size distribution curve are most effective at identifying small particles.

B. Discussion of Project Greater Impacts

This thesis is part of a larger project, which will ideally create a tool that will prove both useful and cost effective for small laboratories seeking shape characterization methods. The combination of computational analysis with the already-simple DLS characterization technique could mean the development of an all-in-one tool which only requires one type of characterization to establish an approximation of the NP shape.

C. Future Work

So far, the work in this project has been lacking in a solid basis of comparison for the shapes of the NPs measured. However, given the observed variations in standard deviations for

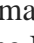
select size peaks, it may be possible to expand upon the DLS data to find the approximate particle shapes by computational means. To explain why, let us explore a thought experiment: imagine you have a sample of non-spherical NPs that have perfectly uniform cylindrical shape. As the particles move in solution, the DLS records the speed at which the light bouncing off the particles changes as the particles shift due to Brownian motion, as explained above. Based on the true dimensions of these cylindrical particles, it would be reasonable to expect the ends of the cylinder to move faster than the length of the cylinders, which would likely be more constrained to the particles that surround it. Additionally, since there would be some sizes recorded for the particles at “in-between” angles, that is, neither exactly perpendicular nor exactly parallel with the laser in orientation, there would be a distribution of recorded sizes that do not correspond with either significant particle dimension. However, it is expected that there would be two significant peaks in recorded hydrodynamic diameter, one of which would correspond to the length of the cylindrical particles, the other to the end faces. Even in this idealized version, though, the dimensions found by the DLS are for the hydrodynamic diameter of the observed dimension, which is the diameter of a perfect sphere that would have the same speed of Brownian motion observed in the tested particle. That means that even if the experimental sample contained only perfectly identical particles, DLS would still not be a sufficient means of collecting dimension data for non-spherical particles. But if a model could predict the scattering data that the DLS instrument would collect based on the known shape of the particles, the shape could be confirmed by the experimental DLS intensity-based size distribution curve. Furthermore, if many models existed to predict the DLS distributions for particles of many shapes, these models may be compared with the experimental DLS data of a sample with an unknown shape in order to find the best match and thus determine the approximate shapes of the samples tested. This method would likely encounter issues with samples that do not have uniform particles, since the various peaks made by the different dimensions of the NPs would be difficult to distinguish for different NP sizes, so it would also be important to either find a synthesis method that results in more consistent NP sizes or filter out large particles to obtain a more uniform sample.

This method of computational vs. experimental data comparison to determine particle shape was used in a study by Bacon, et al. to create a light scattering shape characterization method that they called a “multiangle-multiwavelength spectrophotometer”.⁴⁰ Additionally, the

study by Pencer, et al. which combined SLS and DLS to characterize particle shape included a great deal of the equations and theory behind their models for predicting the relations between data and shape, although their particles were approximately spherical, so theirs was a simpler study of quantifying shape.¹⁵ These studies touch on the use of ellipsoidal NPs, and given the distributions observed in the existing data, it is likely that some of the NPs examined were ellipsoidal. Thus, the above cited papers will be used in combination with existing NP types to determine if they are indeed ellipsoids.

VI. References

- (1) Heron, M. *National Vital Statistics Reports Volume 65, Number 5 June 30, 2016 Deaths: Leading Causes for 2014*; 2016.
- (2) Ott, P. A.; Hodi, F. S.; Kaufman, H. L.; Wigginton, J. M.; Wolchok, J. D. Combination Immunotherapy: A Road Map. <https://doi.org/10.1186/s40425-017-0218-5>.
- (3) Edwards, B. K.; Noone, A.-M.; Mariotto, A. B.; Simard, E. P.; Boscoe, F. P.; Henley, S. J.; Jemal, A.; Cho, H.; Anderson, R. N.; Kohler, B. A.; et al. Annual Report to the Nation on the Status of Cancer, 1975-2010, Featuring Prevalence of Comorbidity and Impact on Survival among Persons with Lung, Colorectal, Breast, or Prostate Cancer. *Cancer* **2014**, *120* (9), 1290–1314. <https://doi.org/10.1002/cncr.28509>.
- (4) Pathak, R. K.; Basu, U.; Ahmad, A.; Sarkar, S.; Kumar, A.; Surnar, B.; Ansari, S.; Wilczek, K.; Ivan, M. E.; Marples, B.; et al. A Designer Bow-Tie Combination Therapeutic Platform: An Approach to Resistant Cancer Treatment by Simultaneous Delivery of Cytotoxic and Anti-Inflammatory Agents and Radiation. *Biomaterials* **2018**, *187*, 117–129. <https://doi.org/10.1016/j.biomaterials.2018.08.062>.
- (5) Sailor, M. J.; Park, J.-H. H. *Hybrid Nanoparticles for Detection and Treatment of Cancer*; 2012; Vol. 24, pp 3779–3802. <https://doi.org/10.1002/adma.201200653>.
- (6) *Intracellular Delivery Fundamentals and Applications*; Prokop, A., Ferrari, M., Eds.; Springer Netherlands, 2011.
- (7) Bergamo, A.; Dyson, P. J.; Sava, G. The Mechanism of Tumour Cell Death by Metal-Based Anticancer Drugs Is Not Only a Matter of DNA Interactions. *Coord. Chem. Rev.* **2018**, *360*, 17–33. <https://doi.org/10.1016/j.ccr.2018.01.009>.
- (8) Tinke, A. P.; Govoreanu, R.; Weuts, I.; Vanhoutte, K.; De Smaele, D. A Review of Underlying Fundamentals in a Wet Dispersion Size Analysis of Powders. *Powder Technol.* **2009**, *196*, 102–114. <https://doi.org/10.1016/j.powtec.2009.08.005>.
- (9) Bhattacharjee, S. DLS and Zeta Potential – What They Are and What They Are Not? *J. Control. Release* **2016**, *235*, 337–351. <https://doi.org/10.1016/j.jconrel.2016.06.017>.
- (10) Wei, S.; Li, A.; Liu, J.-C.; Li, Z.; Chen, W.; Gong, Y.; Zhang, Q.; Cheong, W.-C.; Wang, Y.; Zheng, L.; et al. Direct Observation of Noble Metal Nanoparticles Transforming to

- Thermally Stable Single Atoms. *Nat. Nanotechnol.* **2018**, *13*, 856–863.
<https://doi.org/10.1038/s41565-018-0197-9>.
- (11) Anselmo, A. C.; Zhang, M.; Kumar, S.; Vogus, D. R.; Menegatti, S.; Helgeson, M. E.; Mitragotri, S. Elasticity of Nanoparticles Influences Their Blood Circulation, Phagocytosis, Endocytosis, and Targeting. *ACS Nano* **2015**, *9* (3), 3169–3177.
<https://doi.org/10.1021/acsnano.5b00147>.
 - (12) Hu, Q.; Chen, Q.; Gu, Z. Advances in Transformable Drug Delivery Systems. *Biomaterials* **2018**, *178*, 546–558. <https://doi.org/10.1016/j.biomaterials.2018.03.056>.
 - (13) Kaszuba, M. A basic introduction to Dynamic Light Scattering (DLS) for particle size analysis <https://www.malvernpanalytical.com/en/learn/events-and-training/webinars/W180201BasicDynamicLightScattering.html> (accessed Mar 21, 2019).
 - (14) Xu, R. Light Scattering: A Review of Particle Characterization Applications. *Particuology* **2015**, *18*, 11–21. <https://doi.org/10.1016/j.partic.2014.05.002>.
 - (15) Pencer, J.; Hallett, F. R. Effects of Vesicle Size and Shape on Static and Dynamic Light Scattering Measurements. *Langmuir* **2003**, *19*, 7488–7497.
<https://doi.org/10.1021/la0345439>.
 - (16) Li, Z.; Zhang, B.; Song, Y.; Xue, Y.; Wu, L.; Zhang, W. Single Molecule Study on Polymer-Nanoparticle Interactions: The Particle Shape Matters. *Langmuir* **2017**, *33*, 42.
<https://doi.org/10.1021/acs.langmuir.7b01698>.
 - (17) Palchoudhury, S.; Arabshahi, A.; Gharge, U.; Albattah, A.; George, O.; Foster, Y. Integrated Experimental and Computational Approach for Nanoparticle Flow Analysis. *Phys. Lett. A* **2019**. <https://doi.org/10.1016/j.physleta.2019.02.020>.
 - (18) Liljeström, V.; Mikkilä, J.; Kostianen, M. A. Self-Assembly and Modular Functionalization of Three-Dimensional Crystals from Oppositely Charged Proteins. *Nat. Commun.* **2014**. <https://doi.org/10.1038/ncomms5445>.
 - (19) Chang, Y.; He, L.; Li, Z.; Zeng, L.; Song, Z.; Li, P.; Chan, L.; You, Y.; Yu, X.-F.; Chu, P. K.; et al. Designing Core–Shell Gold and Selenium Nanocomposites for Cancer Radiochemotherapy. **2017**. <https://doi.org/10.1021/acsnano.7b01346>.
 - (20) Nanomaterials,  Jones, M. R.; Seeman, N. C.; Mirkin, C. A. Programmable Materials and the Nature of the DNA Bond. *Science* (80-.). **2015**, *347* (6224), 840.
<https://doi.org/10.1126/science.1260901>.
 - (21) Martchenko, I.; Dietsch, H.; Moitzi, C.; Schurtenberger, P. Hydrodynamic Properties of Magnetic Nanoparticles with Tunable Shape Anisotropy: Prediction and Experimental Verification. *J. Phys. Chem. B* **2011**, *115*, 14838–14845.
<https://doi.org/10.1021/jp2078264>.
 - (22) Schrofel, A.; Kratosova, G. Biosynthesis of Metallic Nanoparticles and Their Applications. In *Intracellular Delivery Fundamentals and Applications*; 2011; pp 373–409. https://doi.org/10.1007/978-94-007-1248-5_14.
 - (23) Palchoudhury, S.; Hyder, F.; Vanderlick, T. K.; Geerts, N. Water-Soluble Anisotropic Iron

- Oxide Nanoparticles: Dextran-Coated Crystalline Nanoplates and Nanoflowers. *Part. Sci. Technol.* **2014**, *32* (3), 224–233. <https://doi.org/10.1080/02726351.2013.850460>.
- (24) Palchoudhury, S.; Xu, Y.; Goodwin, J.; Bao, Y. Synthesis of Multiple Platinum-Attached Iron Oxide Nanoparticles †. *J. Mater. Chem.* **2011**, *21*, 3966–3970. <https://doi.org/10.1039/c0jm04148c>.
 - (25) Sun, X.; Guo, S.; Liu, Y.; Sun, S. Dumbbell-like PtPd–Fe₃O₄ Nanoparticles for Enhanced Electrochemical Detection of H₂O₂. *ACS Nano Lett.* **2012**, *12*, 4859–4863. <https://doi.org/10.1021/nl302358e>.
 - (26) Wang, C.; Xu, C.; Zeng, H.; Sun, S. Recent Progress in Syntheses and Applications of Dumbbell-like Nanoparticles **. *Adv Mater* **2009**, *21* (30), 3045–3052. <https://doi.org/10.1002/adma.200900320>.
 - (27) Herrmann, J. F.; Höppener, C. Dumbbell Gold Nanoparticle Dimer Antennas with Advanced Optical Properties. *Beilstein J. Nanotechnol* **2018**, *9*, 2188–2197. <https://doi.org/10.3762/bjnano.9.205>.
 - (28) Xu, C.; Xie, J.; Ho, D.; Wang, C.; Kohler, N.; Walsh, E. G.; Morgan, J. R.; Eugene Chin, Y.; Sun, S.; Xu, C.; et al. Au-Fe₃O₄ Dumbbell Nanoparticles as Dual-Functional Probes**. *Angew. Chem. Int. Ed* **2008**, *47*, 173–176. <https://doi.org/10.1002/anie.200704392>.
 - (29) Li, M.-H. Stimuli-Responsive Polymersomes. In *Intracellular Delivery Fundamentals and Applications*; 2011; pp 291–331. https://doi.org/10.1007/978-94-007-1248-5_11.
 - (30) Gesquiere, A. J.; Jasmin, K.; Topps, M.; Shroff, S.; Ortiz, A. M.; George, O.; Abdellatif, Y.; Ortiz Ortiz, A. M.; Abdellatif, Y. Conjugated Polymer Nanotherapeutics for Next Generation Photodynamic Therapy. *Med. Res. Arch.* **2018**, *6* (2), 1–23.
 - (31) Vanderesse, R.; Barberi-Heyob, M.; Richeter, S.; Raehm, L.; Durand, J.-O.; Vanderesse, R.; Frochot, C.; Barberi-Heyob, M.; Richeter, S.; Raehm, L.; et al. Nanoparticles for Photodynamic Therapy Applications. In *Fundamental Biomedical Technologies*; 2011; Vol. 5, pp 511–565. https://doi.org/10.1007/978-94-007-1248-5_19.
 - (32) Grunes, J.; Zhu, J.; Anderson, E. A.; Somorjai, G. A. Ethylene Hydrogenation over Platinum Nanoparticle Array Model Catalysts Fabricated by Electron Beam Lithography: Determination of Active Metal Surface Area. **2002**. <https://doi.org/10.1021/jp021641e>.
 - (33) Beranek, J.; Imre, D.; Zelenyuk, A. Real-Time Shape-Based Particle Separation and Detailed in Situ Particle Shape Characterization. *Anal. Chem* **2012**, *84*, 39. <https://doi.org/10.1021/ac202235z>.
 - (34) Levin, A. D.; Shmytkova, E. A.; Khlebtsov, B. N. Multipolarization Dynamic Light Scattering of Nonspherical Nanoparticles in Solution. *J. Phys. Chem. C* **2017**, *17*, 3070–3077. <https://doi.org/10.1021/acs.jpcc.6b10226>.
 - (35) Zheng, T.; Bott, S.; Huo, Q. Techniques for Accurate Sizing of Gold Nanoparticles Using Dynamic Light Scattering with Particular Application to Chemical and Biological Sensing Based on Aggregate Formation. *ACS Appl. Mater. Interfaces* **2016**, *8*, 21585–21594. <https://doi.org/10.1021/acsami.6b06903>.

- (36) Abdelmohsen, L. K. E. A.; Rikken, R. S. M.; Christianen, P. C. M.; Van Hest, J. C. M.; Wilson, D. A. Shape Characterization of Polymersome Morphologies via Light Scattering Techniques. **2016**. <https://doi.org/10.1016/j.polymer.2016.06.067>.
- (37) Xu, Y.; Qin, Y.; Palchoudhury, S.; Bao, Y. Water-Soluble Iron Oxide Nanoparticles with High Stability and Selective Surface Functionality. *Langmuir* **2011**, 27 (14), 8990–8997. <https://doi.org/10.1021/la201652h>.
- (38) Palchoudhury, S.; Lead, J. R. A Facile and Cost-Effective Method for Separation of Oil–Water Mixtures Using Polymer-Coated Iron Oxide Nanoparticles. *Environ. Sci. Technol.* **2014**, 48 (24), 14558–14563. <https://doi.org/10.1021/es5037755>.
- (39) Palchoudhury, S.; Jungjohann, K. L.; Weerasena, L.; Arabshahi, A.; Gharge, U.; Albattah, A.; Miller, J.; Patel, K.; Holler, R. A. Enhanced Legume Root Growth with Pre-Soaking in a-Fe₂O₃ Nanoparticle Fertilizer †. **2018**. <https://doi.org/10.1039/c8ra04680h>.
- (40) Bacon, C.; Garcia-Rubio, L. H. *Multiangle-Multiwavelength Detection for Particle Characterization*; 1998.

VII. Acknowledgements

The author acknowledges the funding provided by the 2018 THEC-CEACSE Award for providing the equipment used, as well as the facilities and resources provided by the University of Tennessee at Chattanooga College of Engineering and Computer Science. Additionally, the author would like to acknowledge the help and instruction provided by Russell George regarding Excel Queries and data processing.

VIII. Appendix

A. Safety Measures

Throughout the course of this research project, consistent measures have been taken to ensure safe handling of the chemicals and samples. Chemical-resistant gloves were worn at all times during sample synthesis and data collection. Synthesis was conducted entirely in a fume hood. Additionally, safe clothing was always worn, meaning that all pants were long (no leggings), all shoes were close-toed, and nothing made of exceptionally flammable or flowy materials was worn. Figure 7 below depicts the sample containment methods used.



Figure 9 – Some of the samples made and characterized; IO NP stock solution pictured left, all Au-NP samples pictured right

B. Project Outcomes

This project has been presented in part as a poster at the American Institute of Chemical Engineering 2018 Annual Student Meeting under the title “Effect of Different Ligands on Water-Soluble Iron Oxide Nanoparticle Size”. This project has also been presented in part as a PowerPoint presentation at the 2018 Southern Conference Undergraduate Research Forum under the same title. This project has also contributed in part to the research presented in the paper titled “Integrated Experimental and Computational Approach for Nanoparticle Flow Analysis” published in Physics Letters A on February 19, 2019.¹⁷ Additionally, this project will be presented in part at the 2019 UTC CECS Technology Symposium, and this project will be presented in full at the 2019 UTC Research Dialogues.

C. Raw Data

1. Overall Data & Distributions

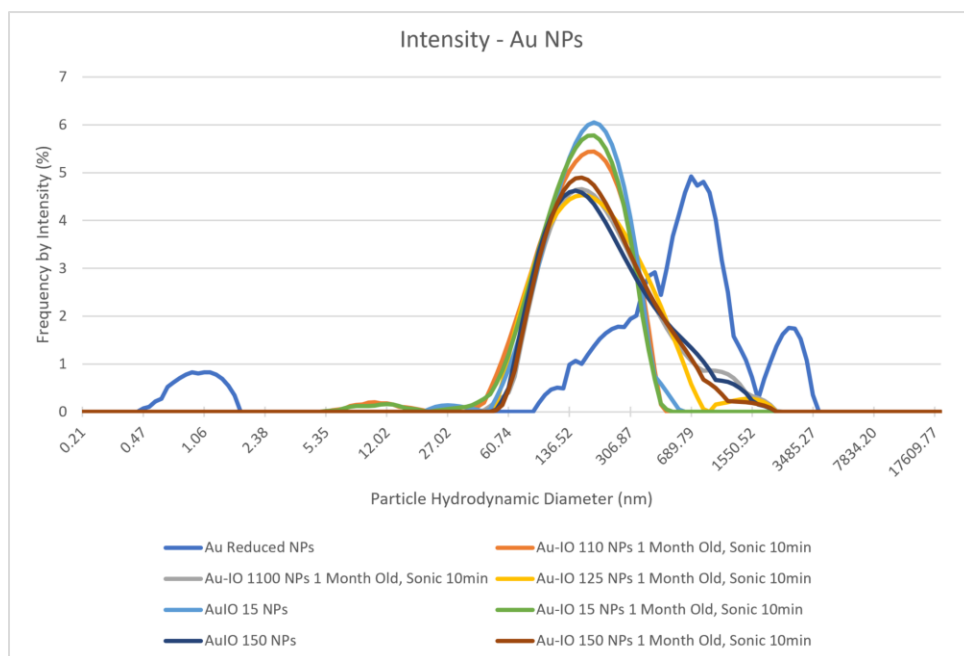


Figure 10 – Intensity-based hydrodynamic diameter distribution curves for Au-IO NPs

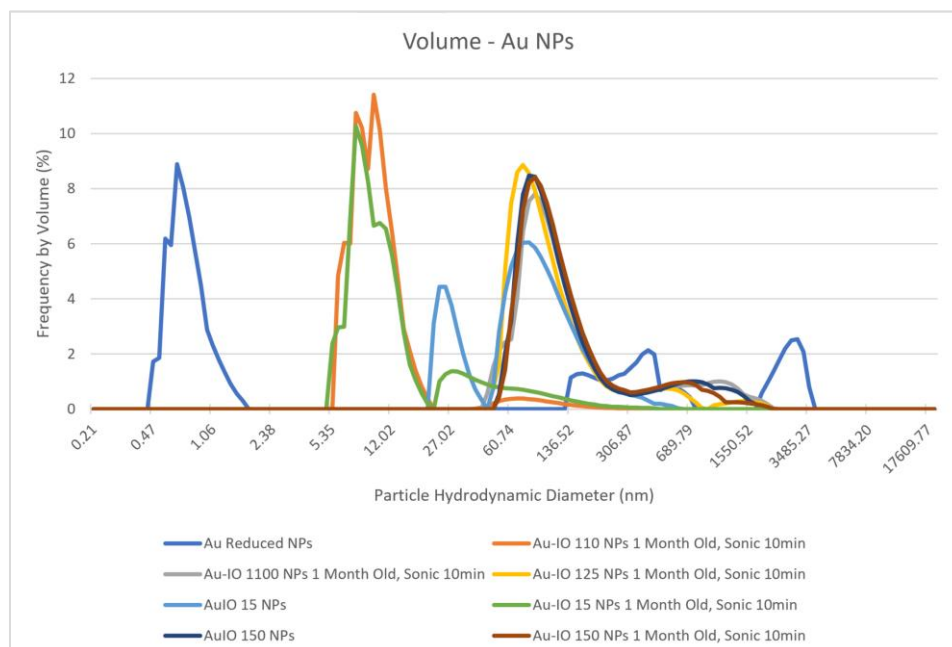


Figure 11 – Volume-based hydrodynamic diameter distribution curves for Au-IO NPs

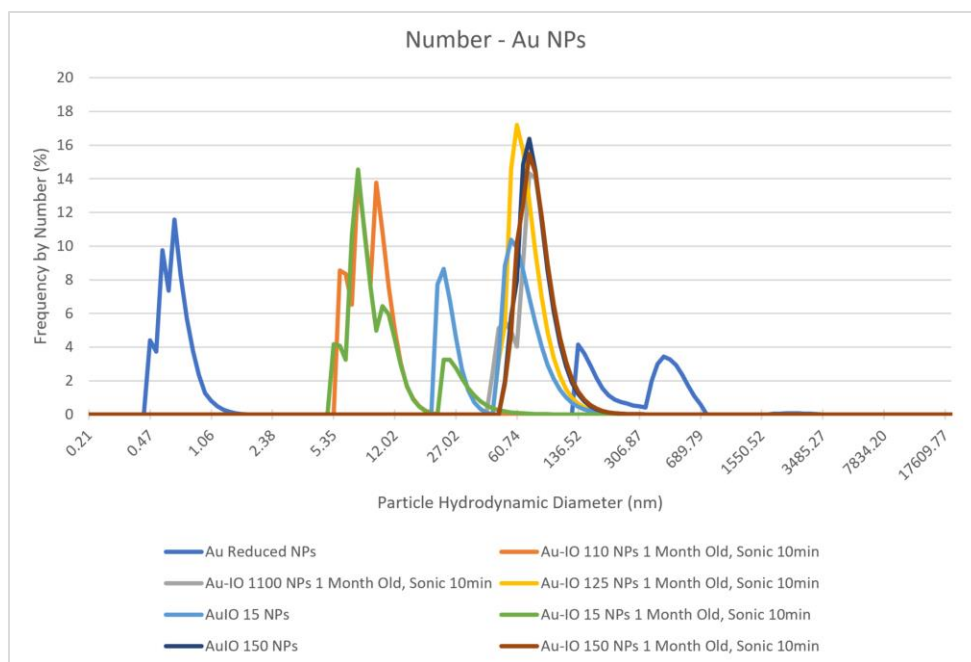


Figure 12 – Number-based hydrodynamic diameter distribution curves for Au-IO NPs

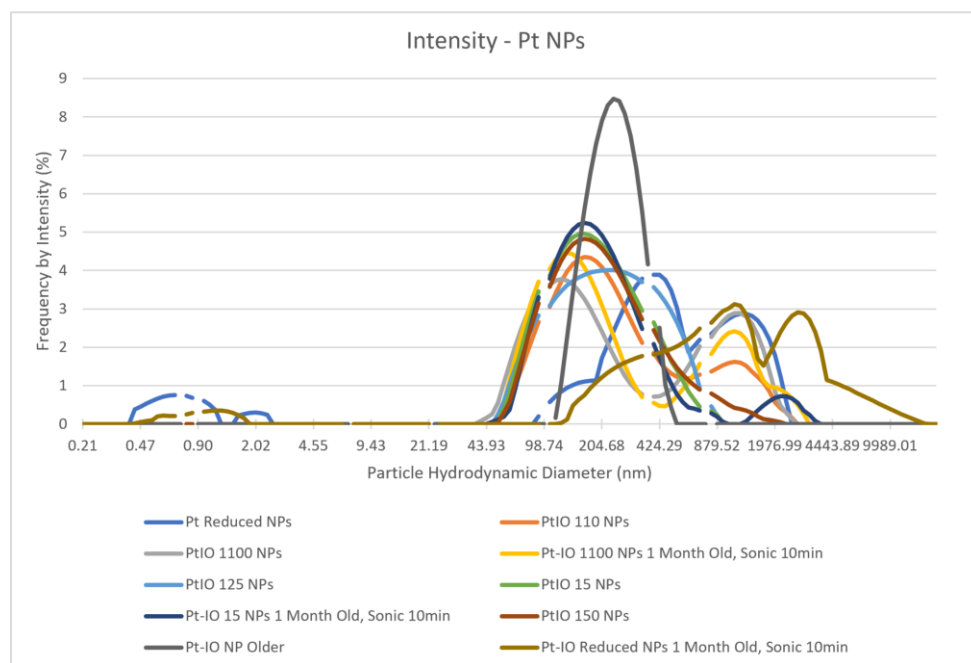


Figure 13 – Intensity-based hydrodynamic diameter distribution curves for Pt-IO NPs

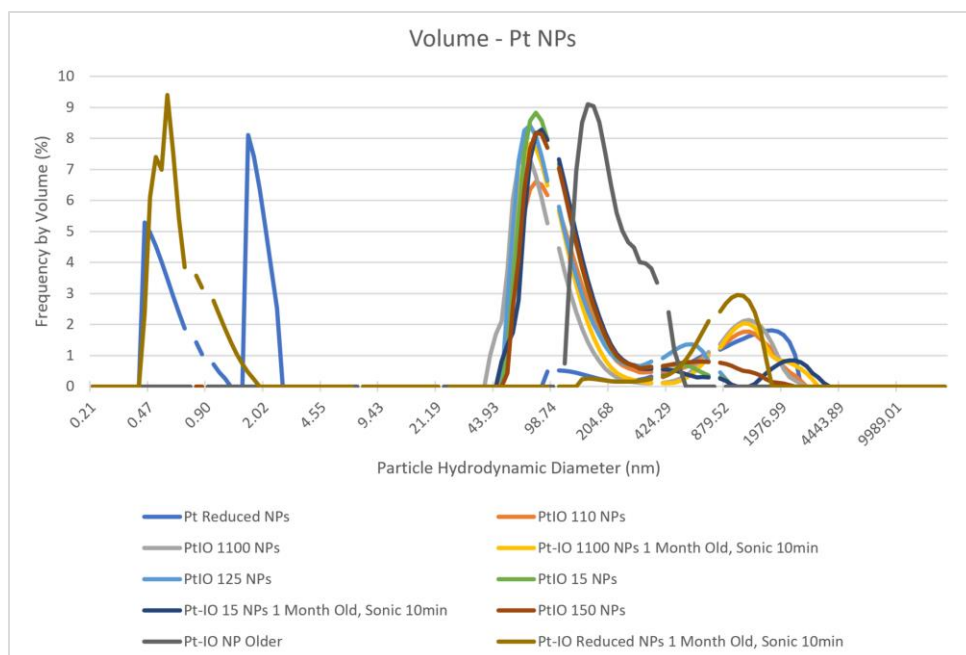


Figure 14 – Volume-based hydrodynamic diameter distribution curves for Pt-IO NPs

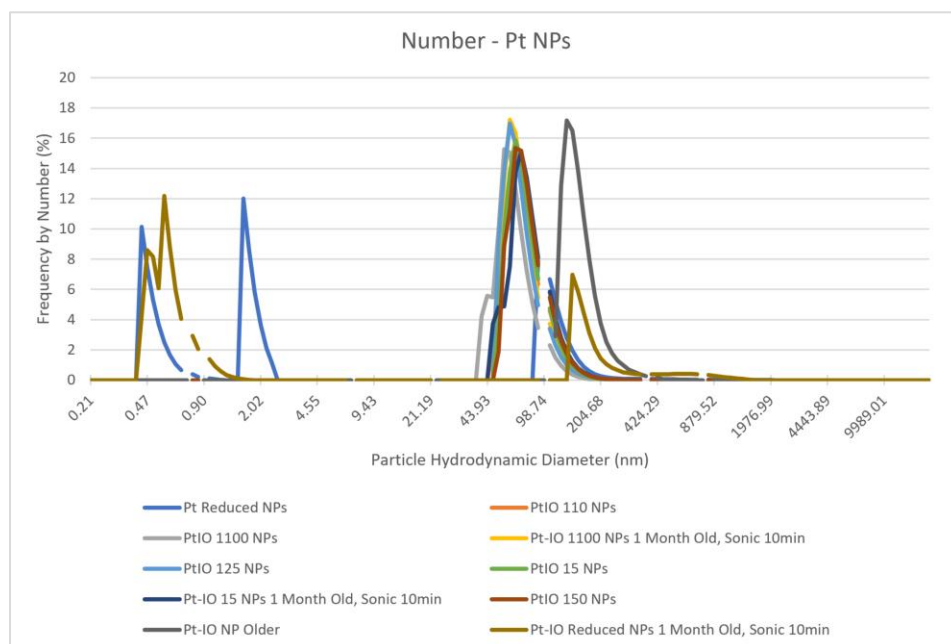


Figure 15 – Number-based hydrodynamic diameter distribution curves for Pt-IO NPs

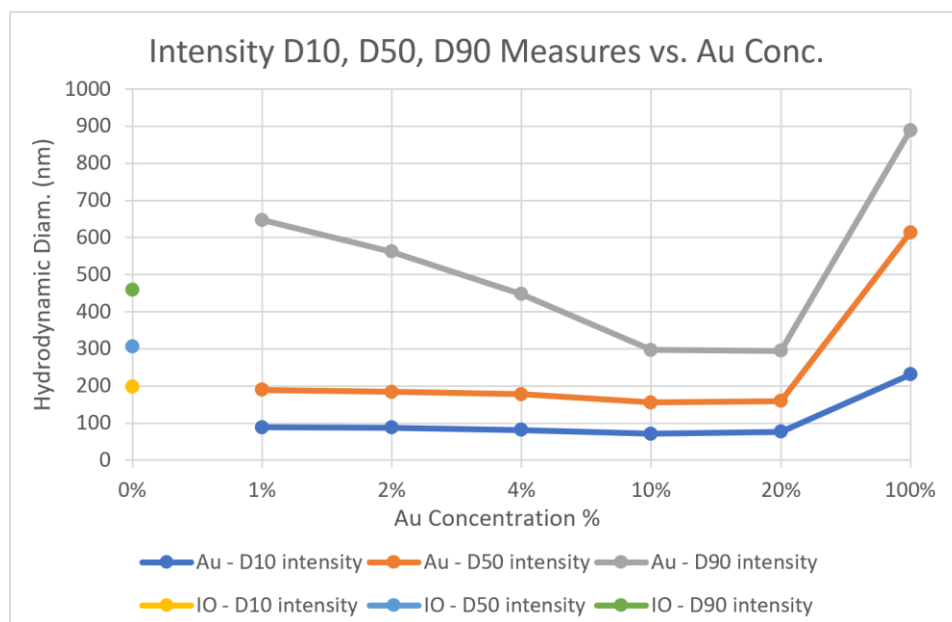


Figure 16 – Trends in Au NP intensity-based distribution data, correlating to the concentration of Au in each NP sample

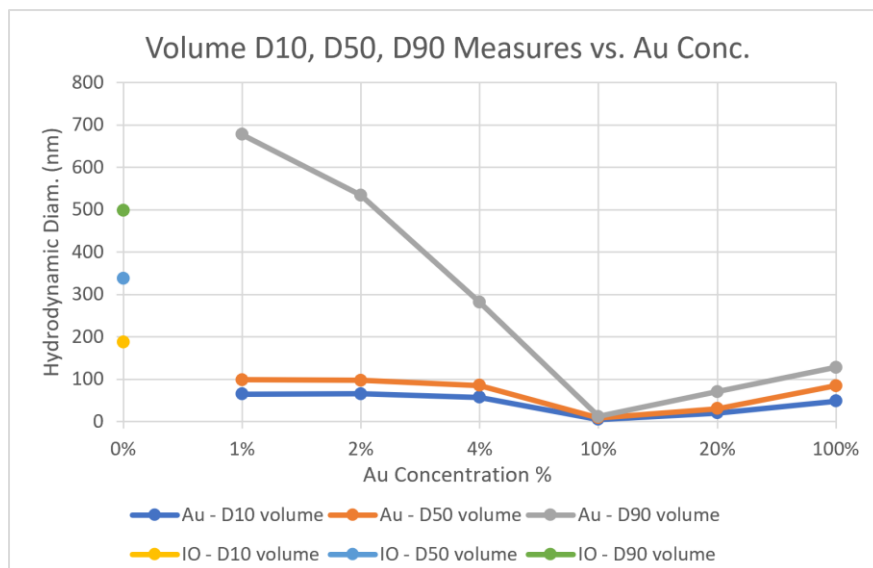


Figure 17 – Trends in Au NP number-based distribution data, correlating to the concentration of Au in each NP sample

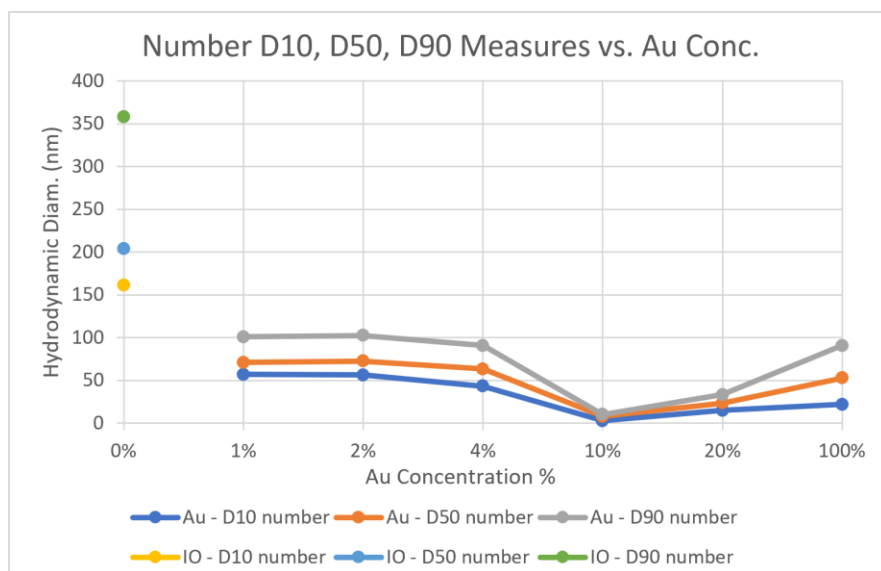


Figure 18 – Trends in Au NP volume-based distribution data, correlating to the concentration of Au in each sample.

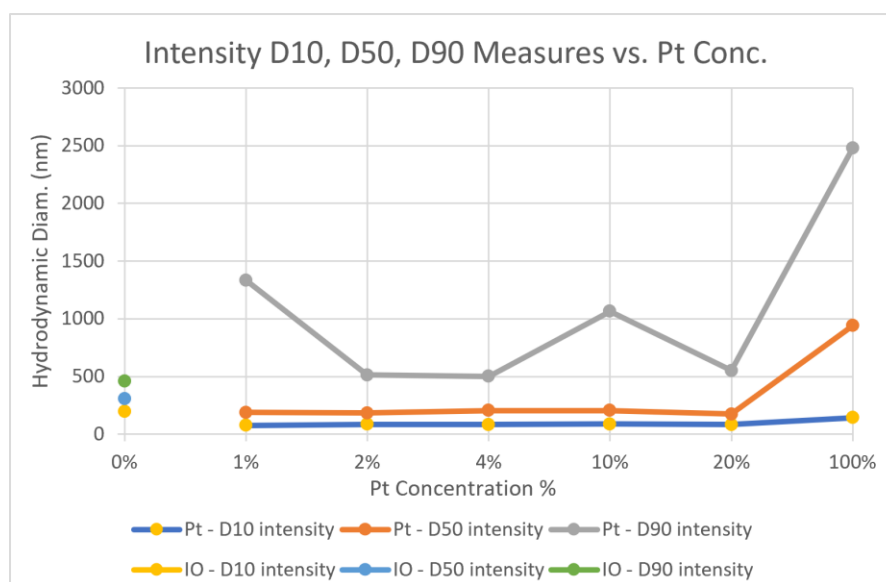


Figure 19 – Trends in Pt NP intensity-based distribution data, correlating to the concentration of Pt in each sample.

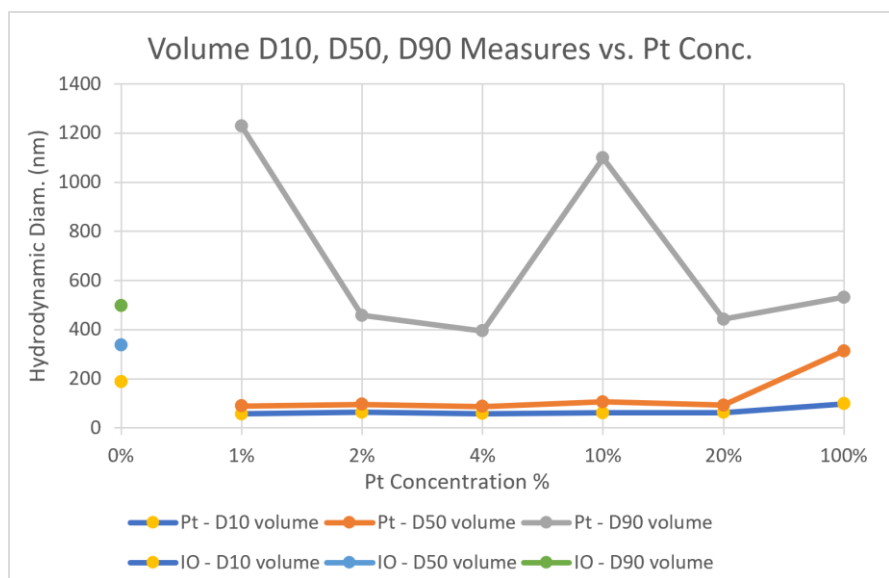


Figure 20 – Trends in Pt NP volume-based distribution data, correlating to the concentration of Pt in each sample.

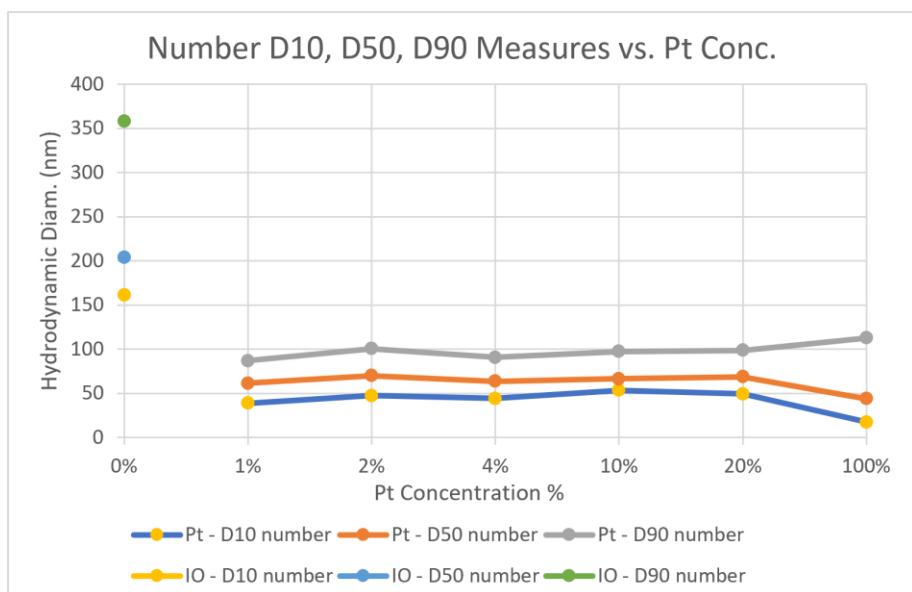


Figure 21 – Trends in Pt NP number-based distribution data, correlating to the concentration of Pt in each sample.

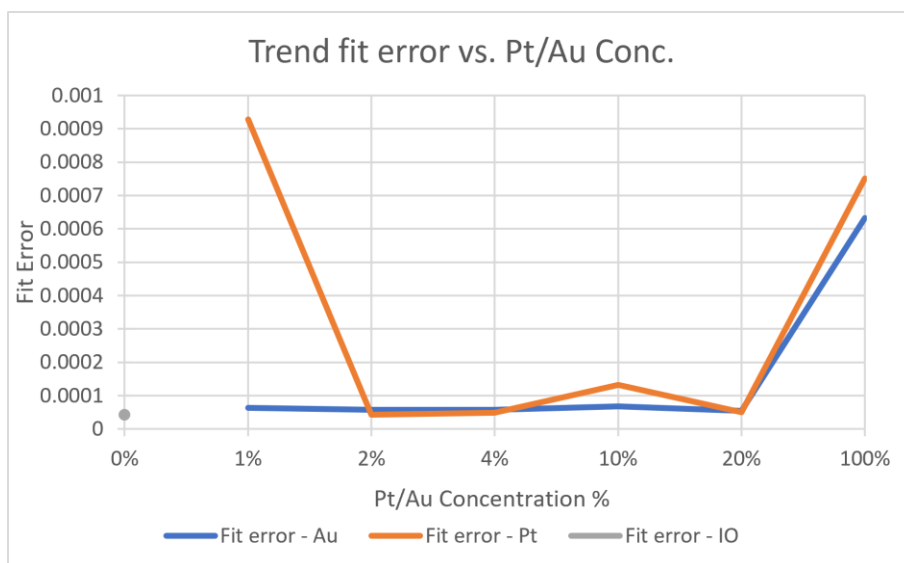


Figure 22 – Trends in the “trend fit error” value calculated automatically by the DLS instrument, correlating to the concentration of Pt/Au in each sample.

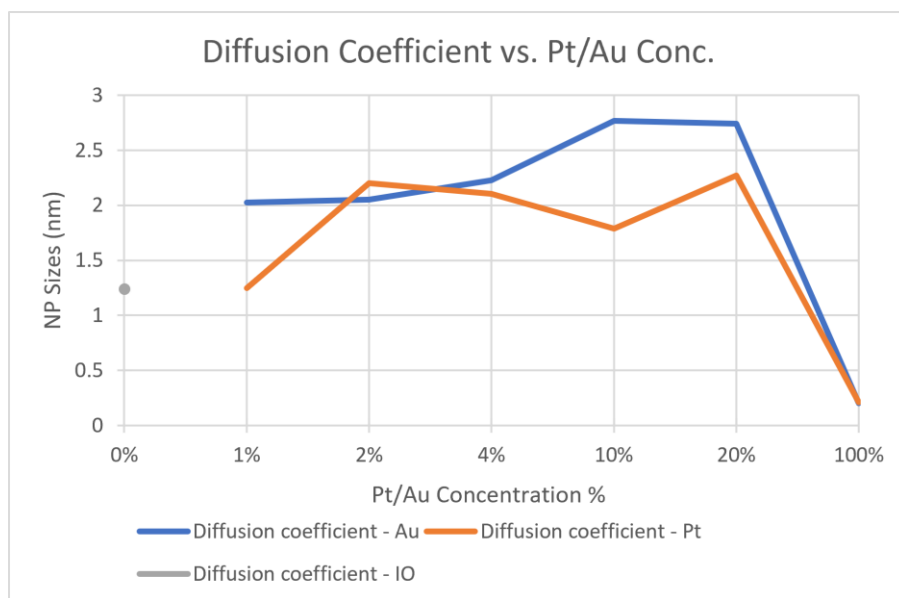


Figure 23 – Trends in the “diffusion coefficient” value calculated automatically by the DLS instrument, correlating to the concentration of Pt/Au in each sample.

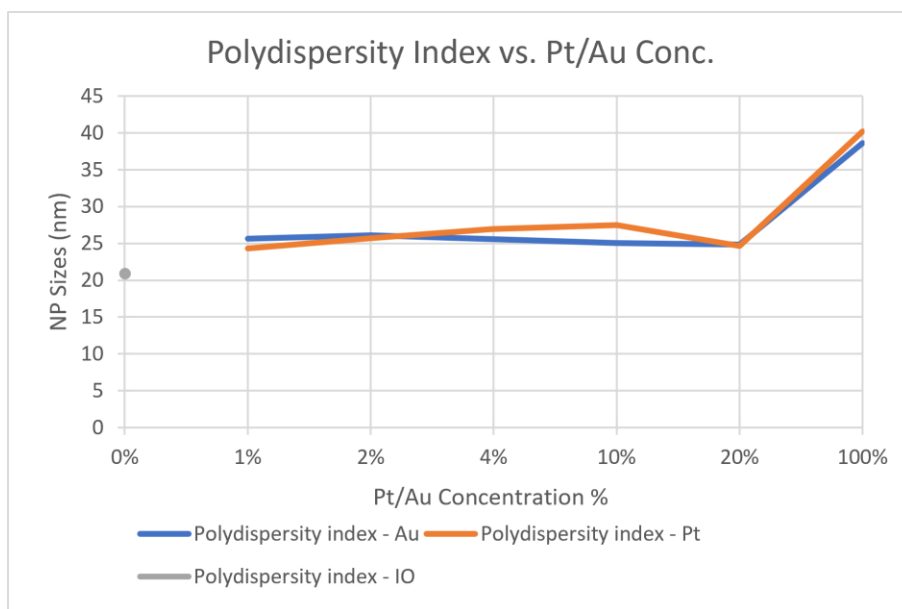


Figure 24 – Trends in the polydispersity index (PDI) value calculated automatically by the DLS instrument, correlating to the concentration of Pt/Au in each sample.

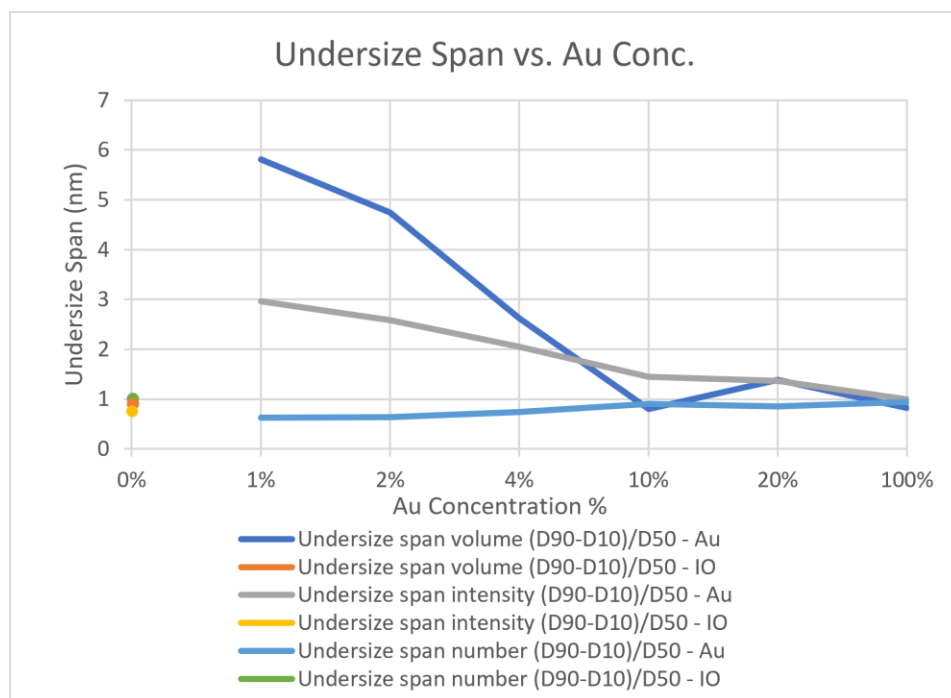


Figure 25 – Intensity, volume, and number-based trends in the undersize span of the Au-IO NPs, correlating to the concentration of Au in each sample. Undersize span is a value derived from the statistical extremes and average values for size, useful for looking at the variety in the data.

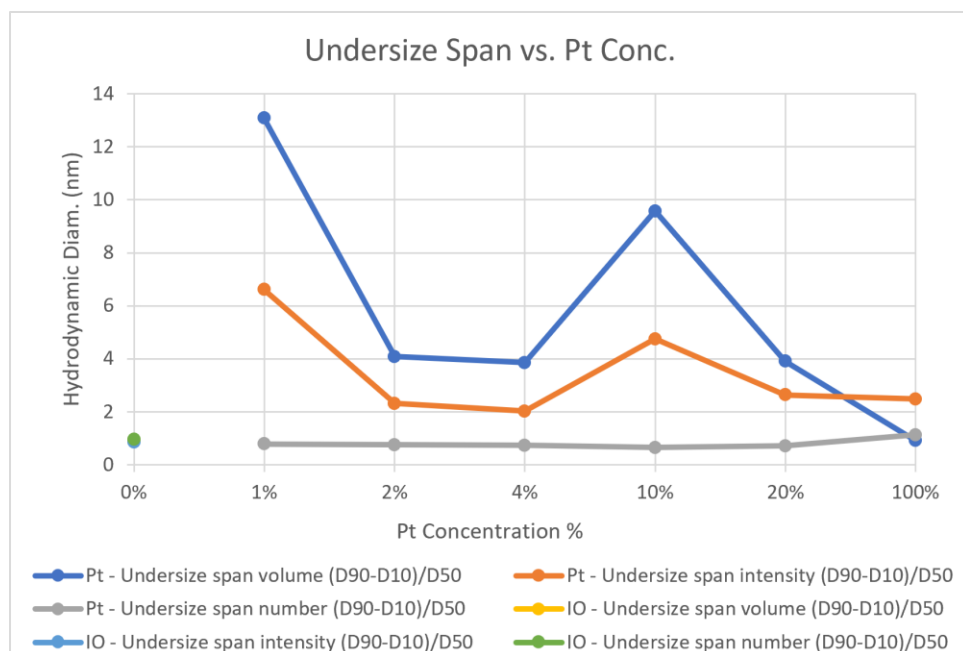


Figure 26 – Intensity, volume, and number-based trends in the undersize span of the Pt-IO NPs, correlating to the concentration of Pt in each sample. Undersize span is a value derived from the statistical extremes and average values for size, useful for looking at the variety in the data.

2. Au NP Standard Deviation Data

The following figures will be in order from the lowest concentration of Au in the NPs to the highest concentration.

Note: the figures for the following Au samples are included in the text: Reduced, 1:5 fresh, 1:5 1 month old

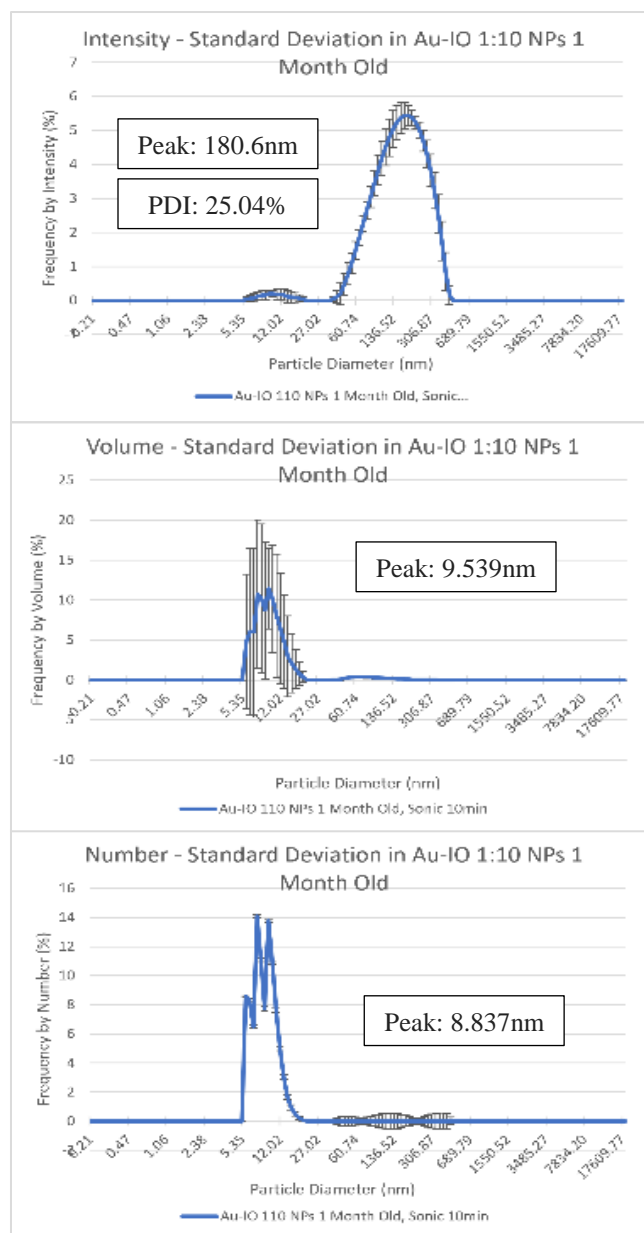


Figure 27 – The intensity, volume, and number-based distributions of hydrodynamic diameter with trends in standard deviation for the Au-IO 1:10, 1 month old sample data

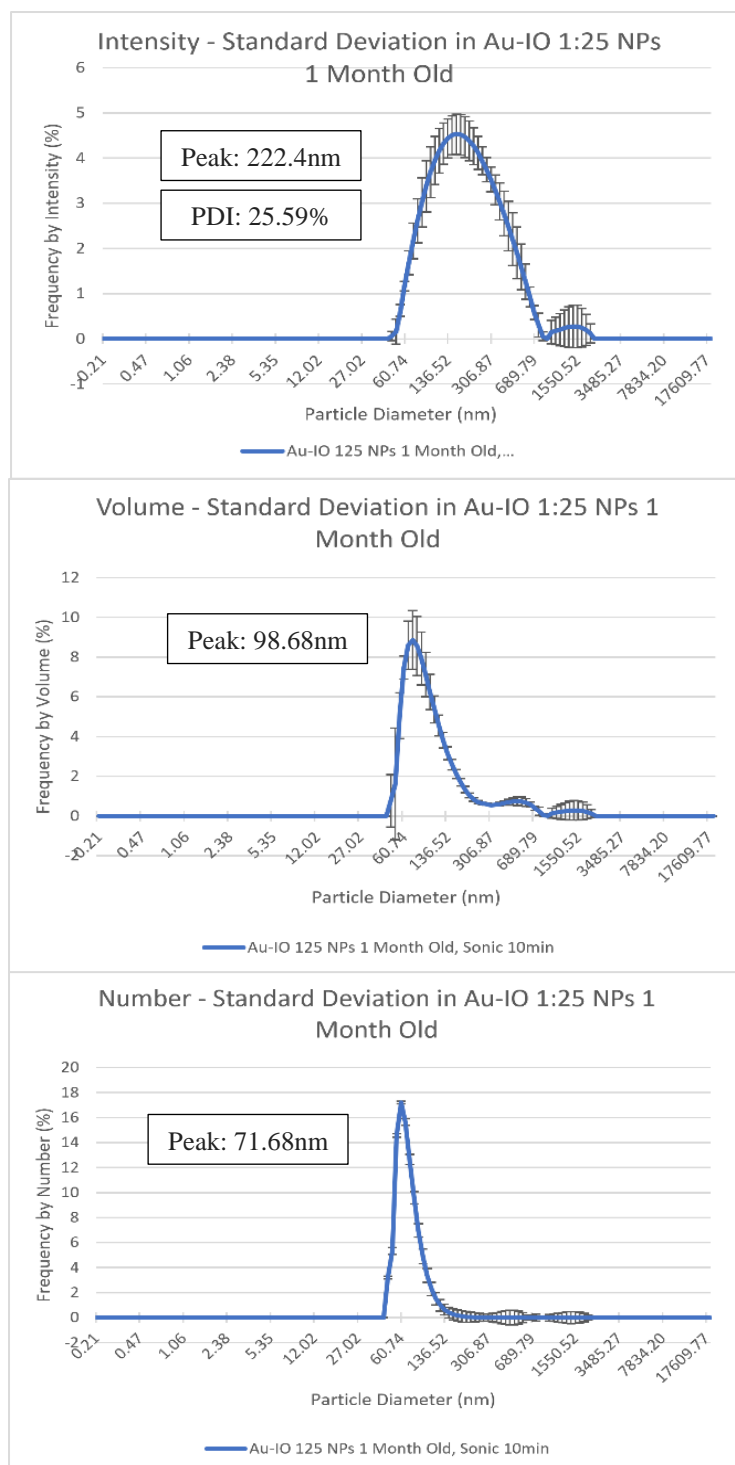


Figure 28 –The intensity, volume, and number-based distributions of hydrodynamic diameter with trends in standard deviation for the Au-IO 1:25, 1 month old sample data

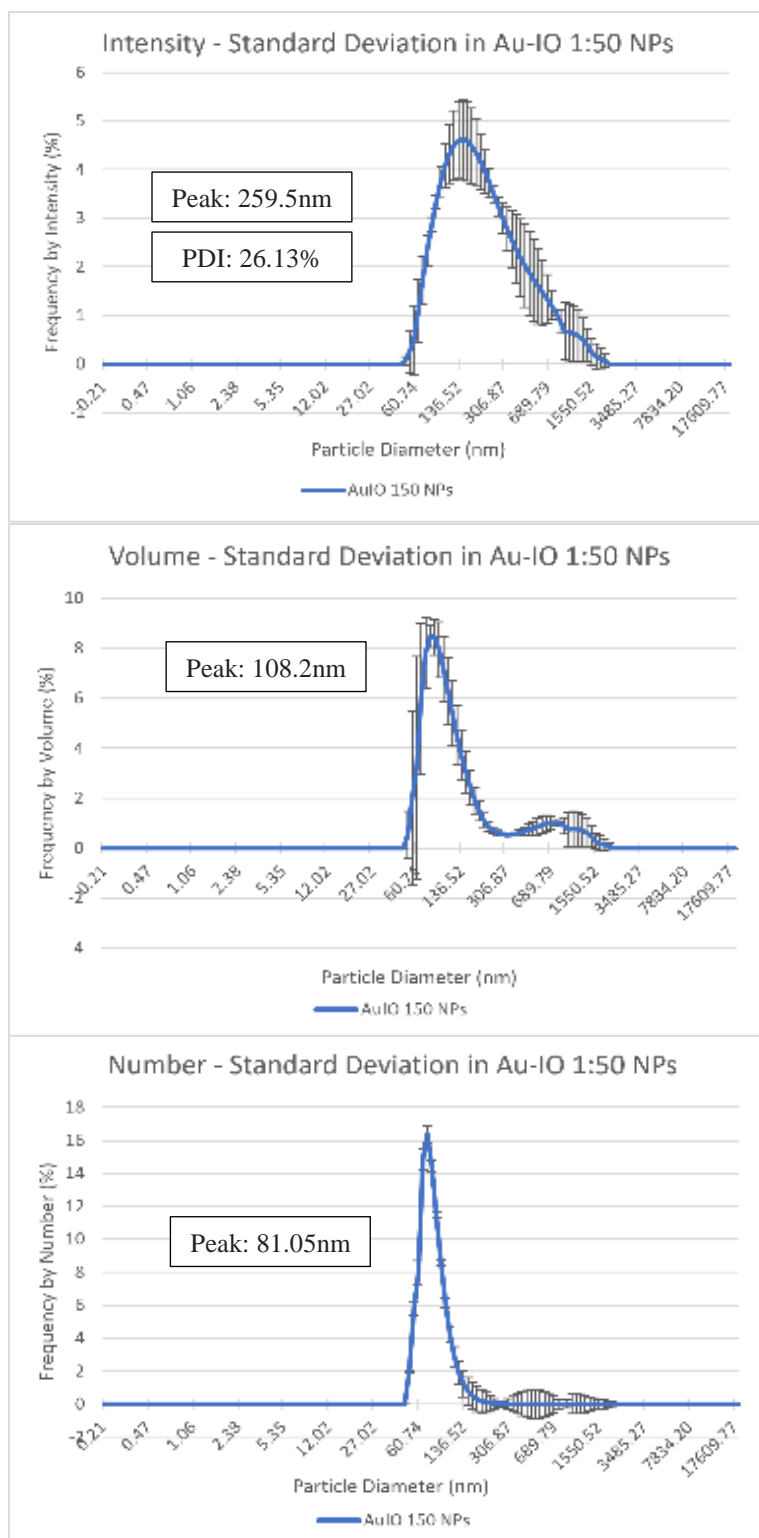


Figure 29 – The intensity, volume, and number-based distributions of hydrodynamic diameter with trends in standard deviation for the Au-IO 1:50 sample data

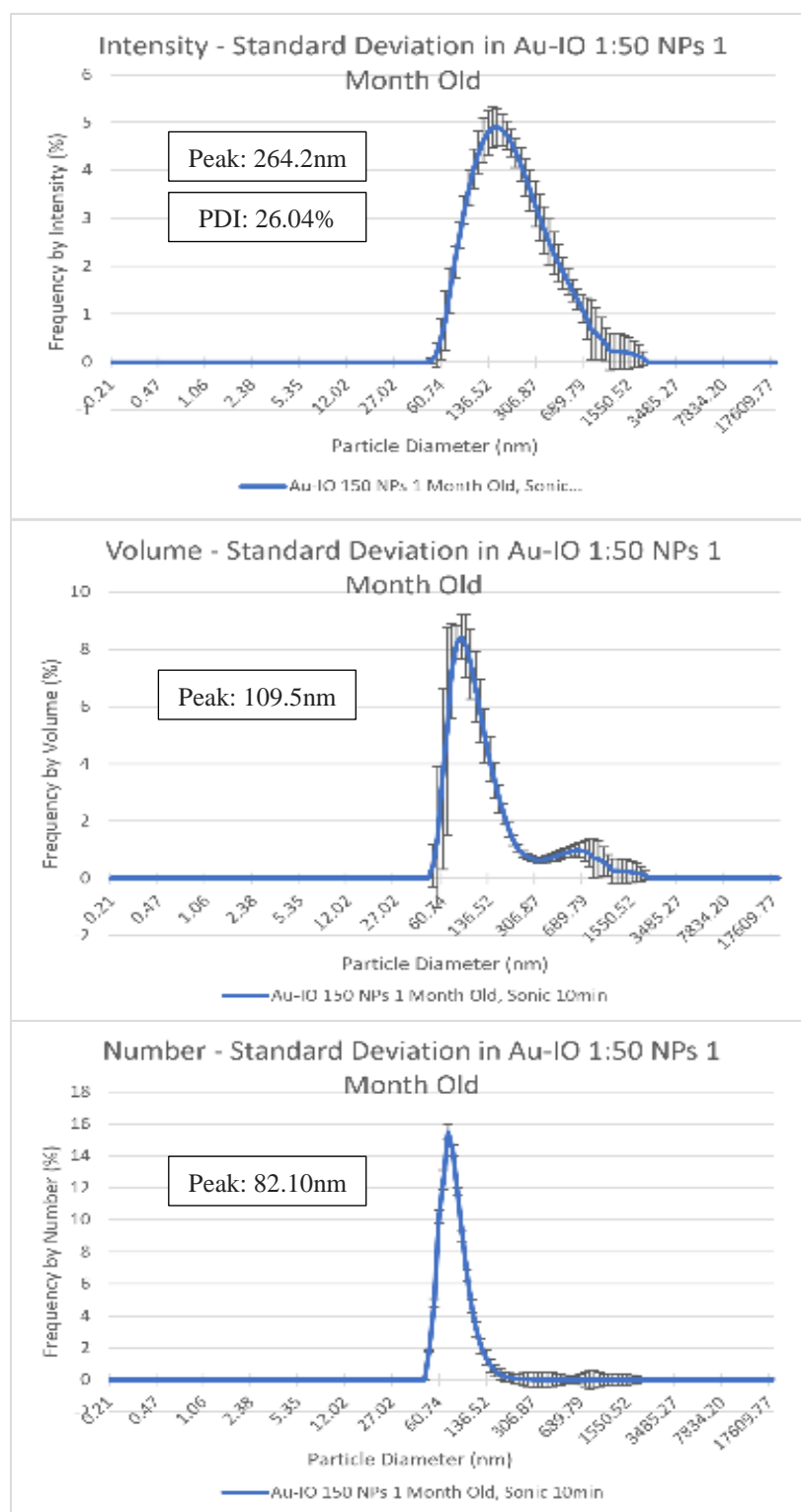


Figure 30 – The intensity, volume, and number-based distributions of hydrodynamic diameter with trends in standard deviation for the Pt-IO 1:50, 1 month old sample data

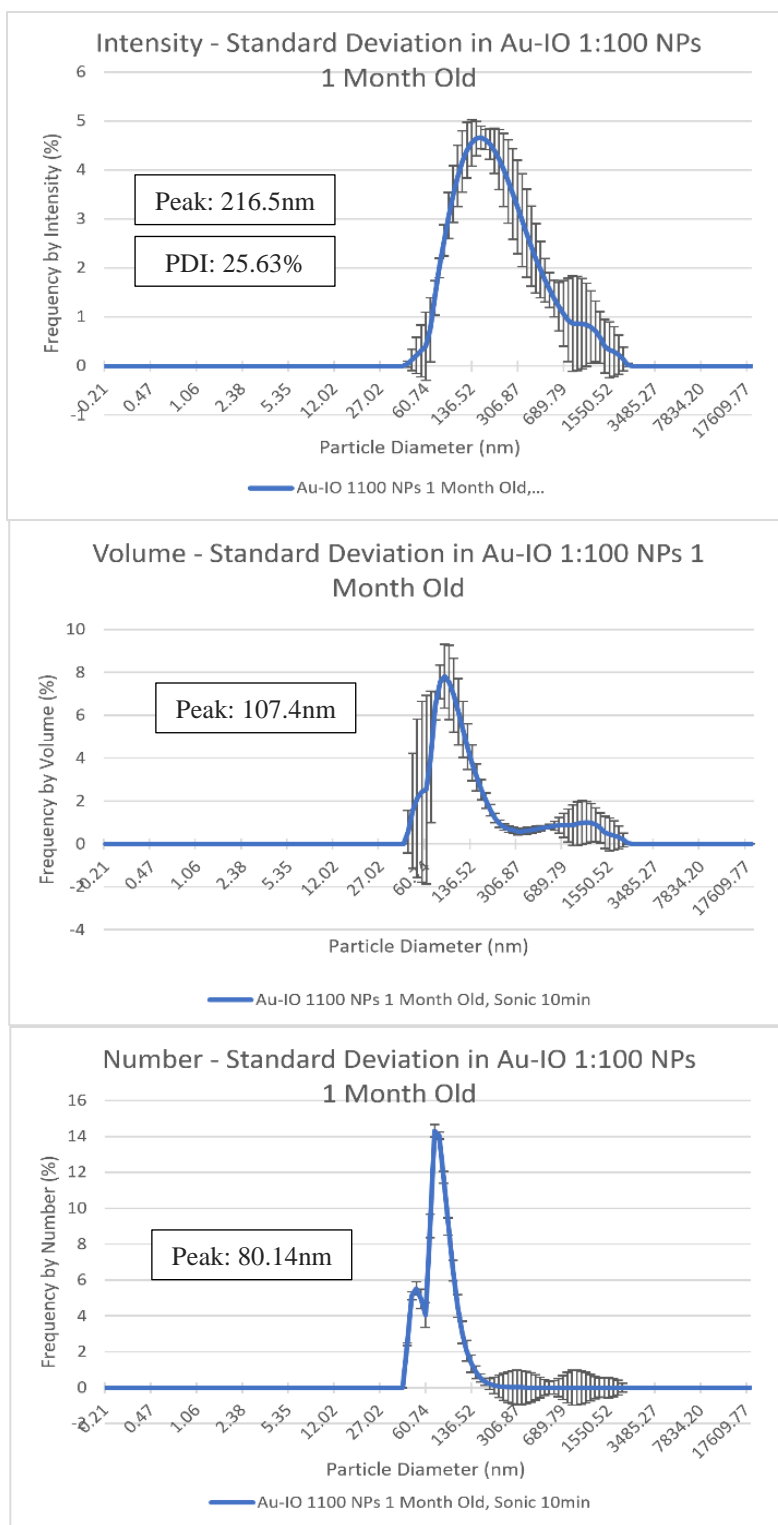


Figure 31 – The intensity, volume, and number-based distributions of hydrodynamic diameter with trends in standard deviation for the Au-IO 1:100, 1 month old sample data

3. Pt NP Standard Deviation Data

Similar to the Au NP data, the following figures will be in order from the highest concentration of Pt in the NPs to the highest concentration.

Note: the figures for the following Pt samples are included in the text: 1:5 fresh, 1:5 1 month old

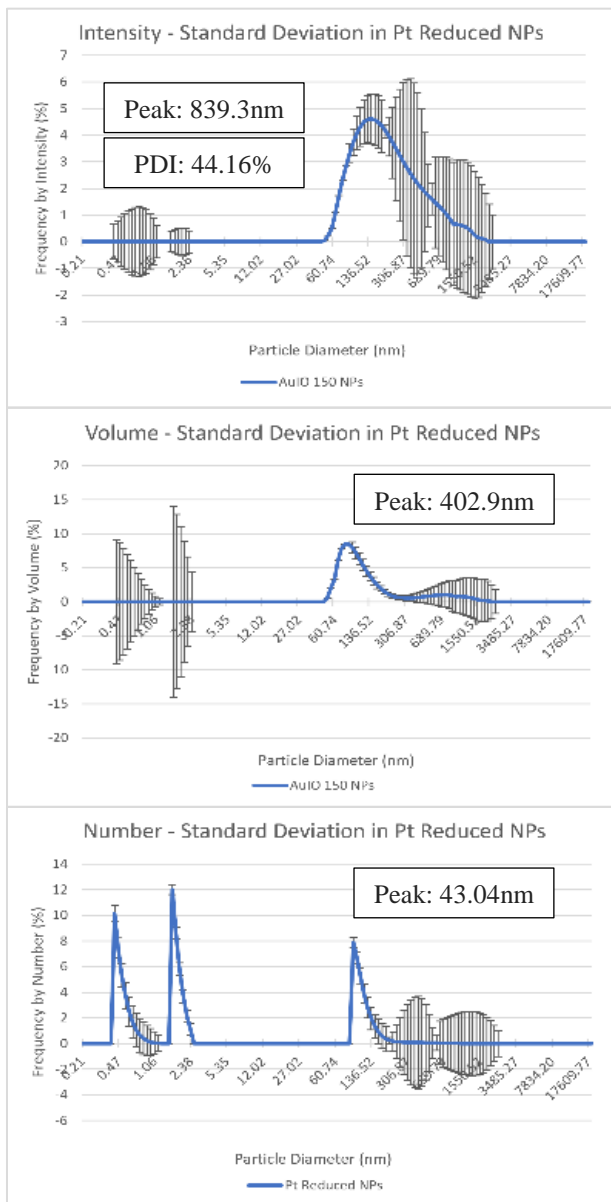


Figure 32 – The intensity, volume, and number-based distributions of hydrodynamic diameter with trends in standard deviation for the Pt Reduced NPs sample data

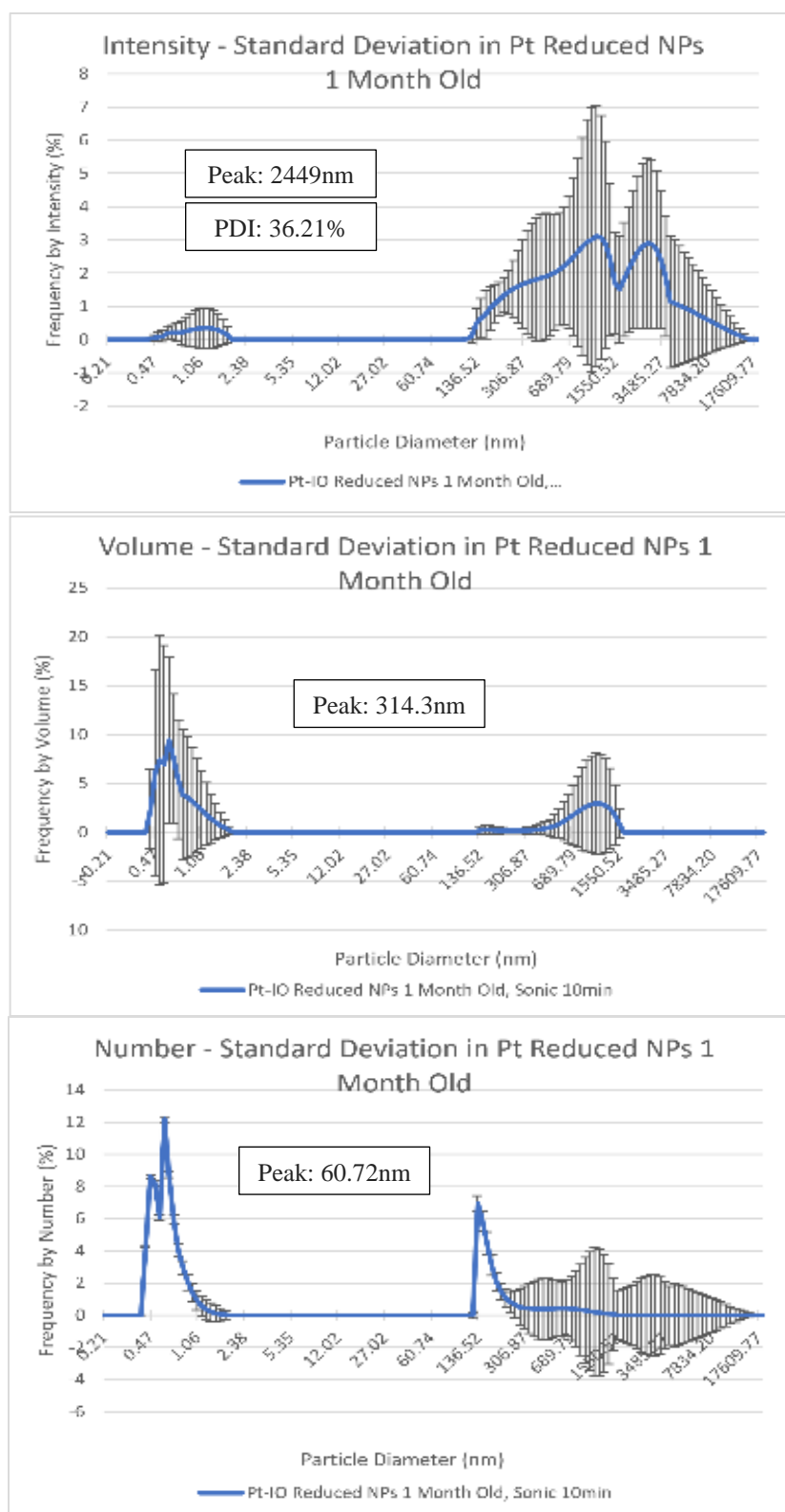


Figure 33 – The intensity, volume, and number-based distributions of hydrodynamic diameter with trends in standard deviation for the Pt Reduced NPs, 1 month old sample data

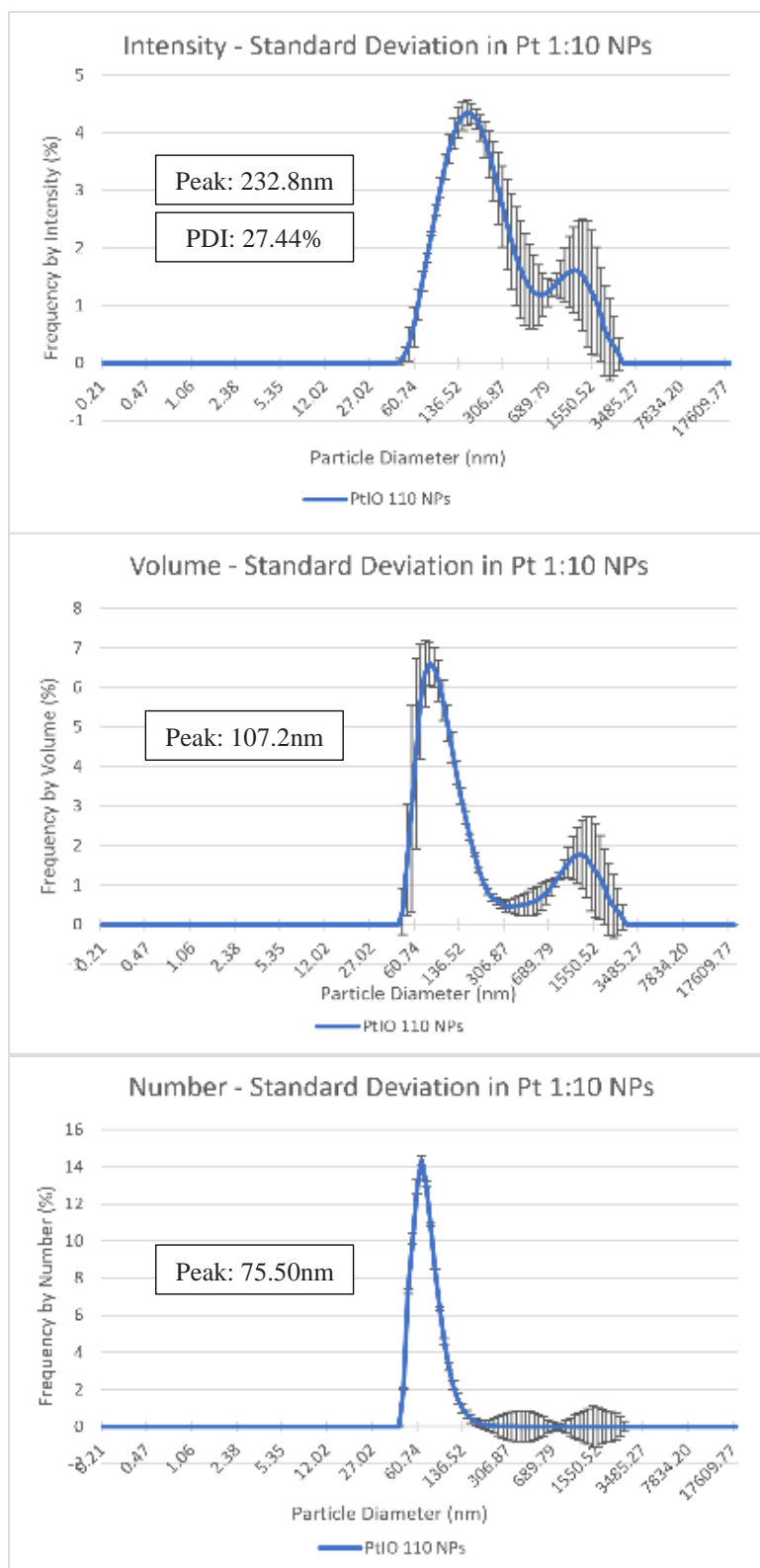


Figure 34 – The intensity, volume, and number-based distributions of hydrodynamic diameter with trends in standard deviation for the Pt-IO 1:10 sample data

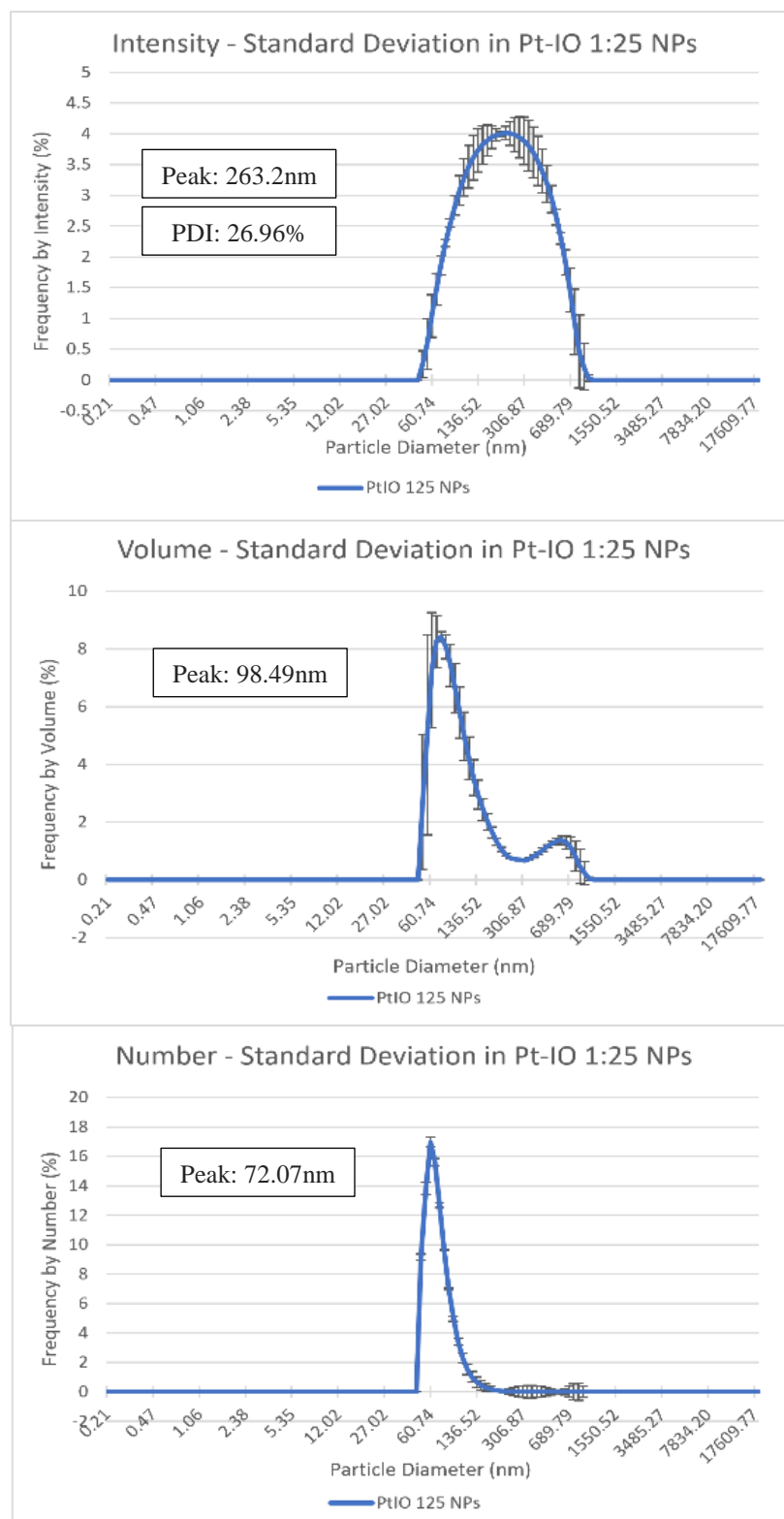


Figure 35 – The intensity, volume, and number-based distributions of hydrodynamic diameter with trends in standard deviation for the Pt-IO 1:25 sample data

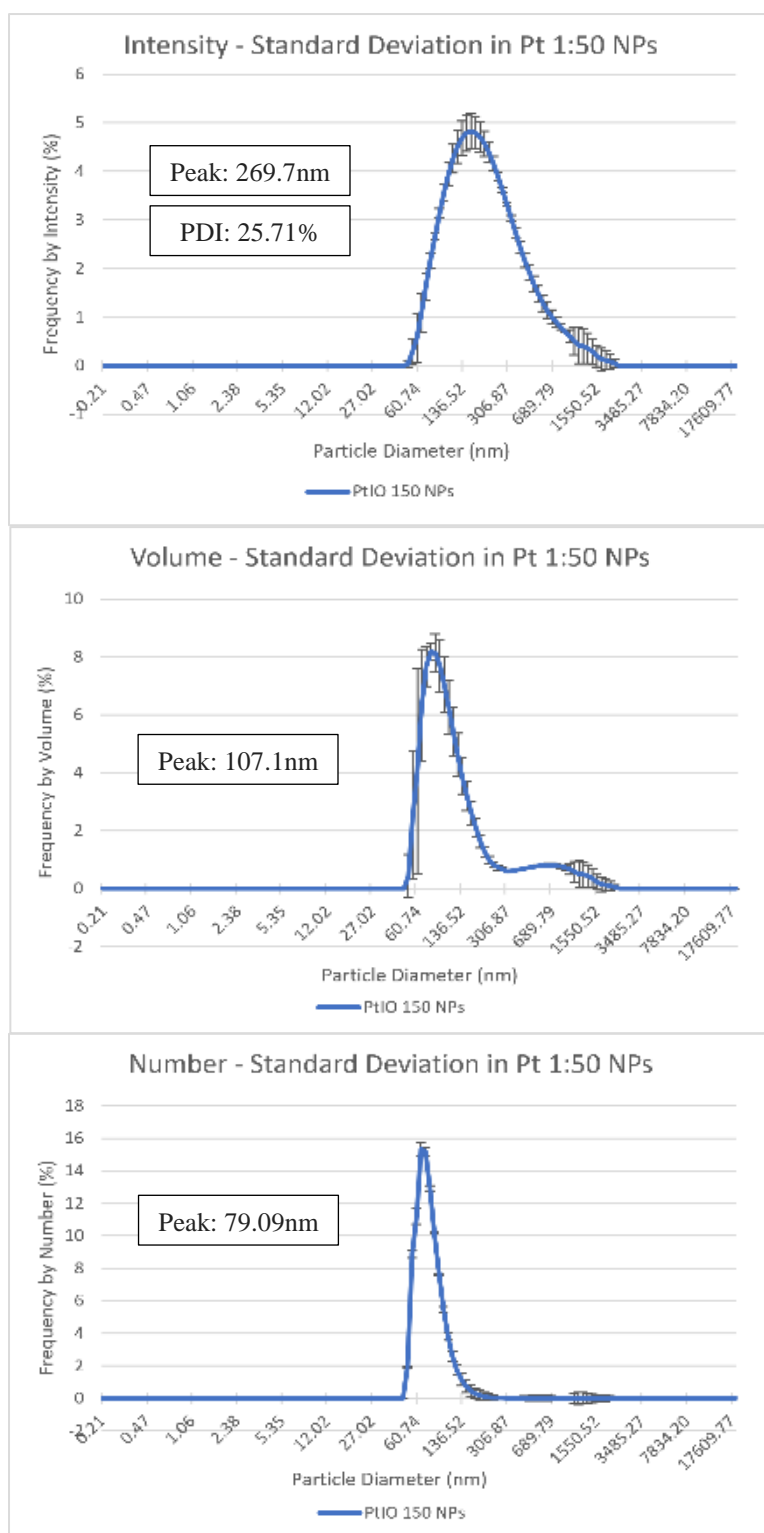


Figure 36 – The intensity, volume, and number-based distributions of hydrodynamic diameter with trends in standard deviation for the Pt-IO 1:50 sample data

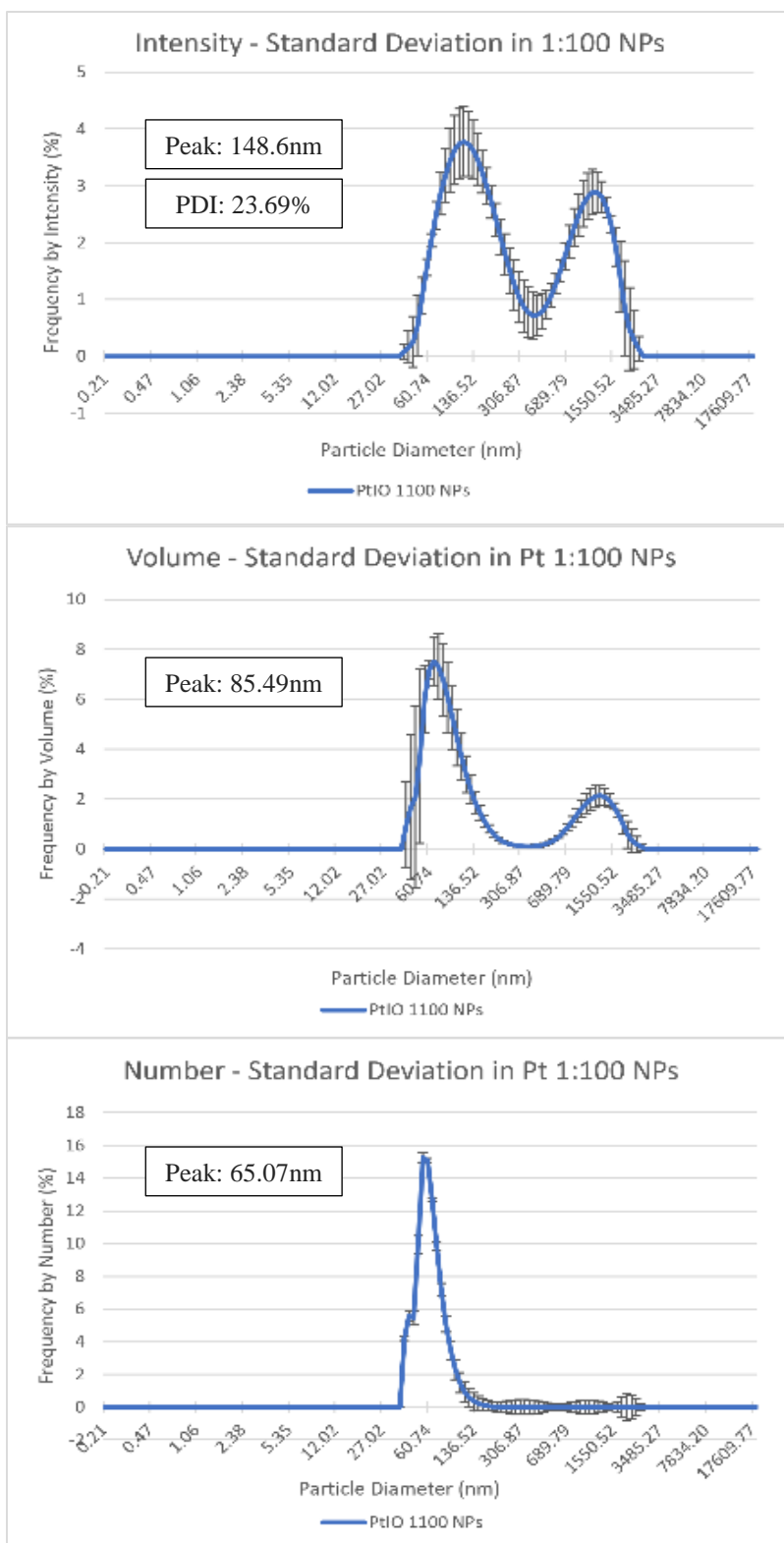


Figure 37 – The intensity, volume, and number-based distributions of hydrodynamic diameter with trends in standard deviation for the Pt-IO 1:100 sample data

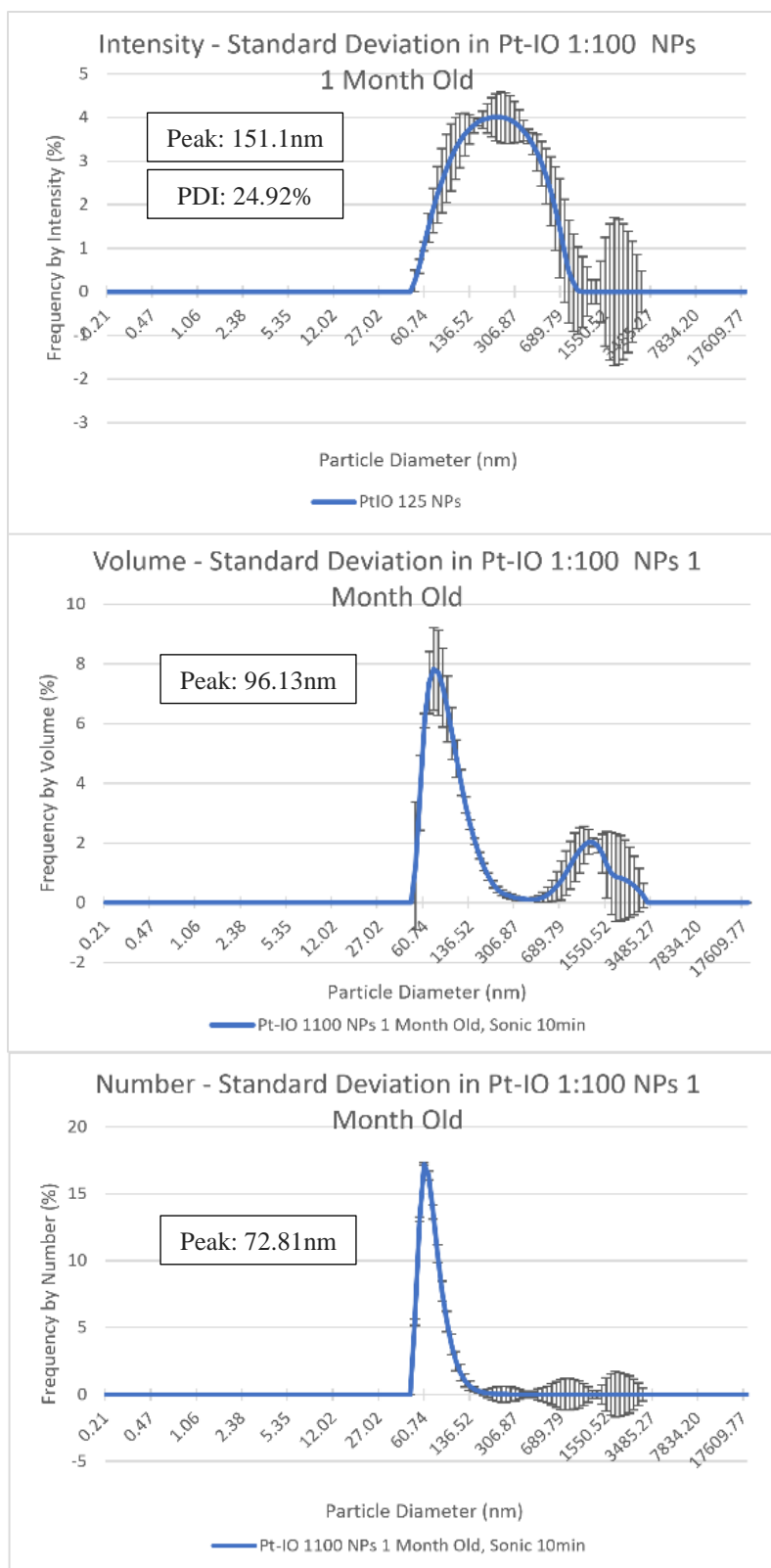


Figure 38 – The intensity, volume, and number-based distributions of hydrodynamic diameter with trends in standard deviation for the Pt-IO 1:100, 1 month old sample data

4. Au NP Standard Deviation Data

Note that the standard deviations could not be calculated because the sample was not measured in triplicate, as the rest of the samples. This sample was measured before measuring in triplicate became standard.

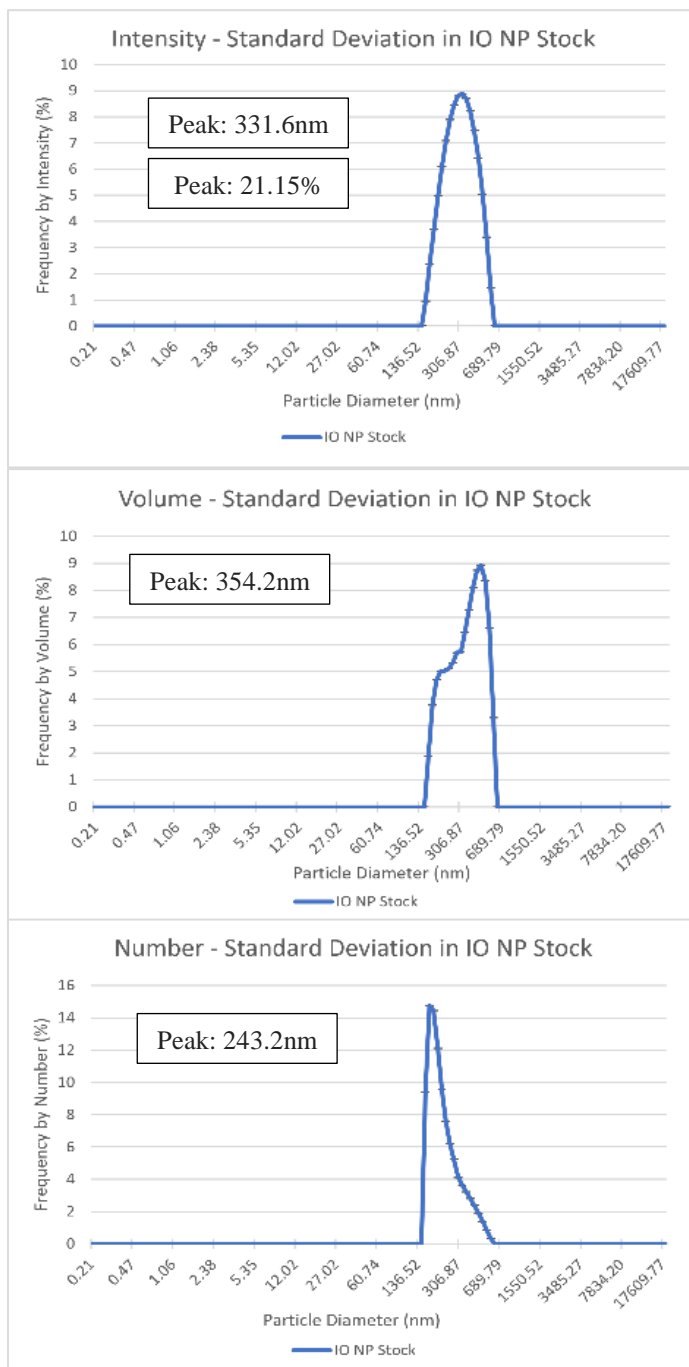


Figure 39 – The intensity, volume, and number-based distributions of hydrodynamic diameter with trends in standard deviation for the IO core NPs sample data